# MASARYKOVA UNIVERZITA

## Přírodovědecká fakulta

### Ústav teoretické fyziky a astrofyziky


BAKALÁŘSKÁ PRÁCE


Brno 2020 Marko Mesarč

MASARYKOVA UNIVERZITA
**Přírodovědecká fakulta**
**Ústav teoretické fyziky a astrofyziky**

# Pozorovatelnost exoplanet v městských podmínkách

BAKALÁŘSKÁ PRÁCE

Marko Mesarč

VEDOUCÍ BAKALÁŘSKÉ PRÁCE:
Mgr. Marek Skarka, Ph.D.

BRNO 2020

## Bibliografický záznam

| | |
|---|---|
| **Autor:** | Marko Mesarč<br>Přírodovědecká fakulta, Masarykova univerzita<br>Ústav teoretické fyziky a astrofyziky |
| **Název práce:** | Pozorovatelnost exoplanet v městských podmínkách |
| **Studijní program:** | Fyzika |
| **Obor:** | Astrofyzika |
| **Vedoucí práce:** | Mgr. Marek Skarka, Ph.D. |
| **Akademický rok:** | 2019/2020 |
| **Počet stran:** | vii + 42 |
| **Klíčová slova:** | CCD fotometrie, exoplanety, otevřená hvězdokupa,<br>M34, pozorovací podmínky |

## Bibliographic record

| | |
|---|---|
| **Author:** | Marko Mesarč<br>Faculty of Science, Masaryk University<br>Department of Theoretical Physics and Astrophysics |
| **Title of Thesis:** | Observability of exoplanets in the city environment |
| **Degree Programme:** | Physics |
| **Field of study:** | Astrophysics |
| **Supervisor:** | Mgr. Marek Skarka, Ph.D. |
| **Academic Year:** | 2019/2020 |
| **Number of Pages:** | vii + 42 |
| **Keywords:** | CCD photometry, exoplanets, open star cluster, M34, observing conditions |

# ABSTRAKT

Cieľom tejto práce je určiť, za akých podmienok sme schopní detekovať planéty mimo Slnečnej sústavy – exoplanéty – v mestských podmienkach Brna. Najefektívnejším spôsobom je do fotometrických dát, nameraných v Brne, umelo vložiť tranzit a následne pomocou programov určiť detekovateľnosť exoplanéty. Pre túto simuláciu boli vybrané exoplanéty s relatívnou hĺbkou tranzitu o veľkosti 2%, 1% a 0,57%. Detekovateľný tranzit môže byť ovplyvnený jasnosťou hviezdy, farbou hviezdy v závislosti na meniacej sa výške nad obzorom a gradientom osvetlenia čipu spôsobený Mesiacom či svetelným znečistením. A práve závislosť na jasnosti, farbe a vzdialenosti hviezd overia magnitúdový, farebný a vzdialenostný test počas troch rozdielných nocí. Pre CCD fotometriu bola zvolená otvorená hviezdokopa M34, kvôli rôznorodosti hviezd, ich ideálnej vzájomnej vzdialenosti a vysokou kulmináciou v čase pozorovania. Meranie prebiehalo pomocou teleskopu o priemere 0,6 metra na Observatóriu Masarykovej Univerzity pri 20 sekundovej expozícii v *R* filtry. Zistili sme, že exoplanéta s relatívnou hĺbkou tranzitu 2% bude detekovateľná pri všetkých zvolených hviezdach (9 mag – 13,6 mag) počas každej z nocí. Exoplanéta s relatívnou hĺbkou tranzitu 1% má najširší tranzit zo zvolených exoplanét (0,11 dňa), ktorý spôsobil to, že bola ťažšie detekovateľná najmä počas nocí so zvýšeným rozptylom v dátach spôsobený oblačnosťou. Posledná z exoplanét s relatívnou hĺbkou tranzitu 0,57% bola najlepšie detekovateľná počas noci 3, kvôli najlepším pozorovacím podmienkam. Zo získaných výsledkov môžeme usúdiť, že detekovateľnosť tranzitu najviac ovplyvňuje pomer signál/šum, závisiaci od seeingu, a pozorovacie podmienky, najmä stálosť rýchlosti vetra a stabilita tlaku.

## ABSTRACT

The main goal of this thesis is to determine the observable conditions under which we are able to detect planets outside of our Solar System – exoplanets – in the city environment of Brno. The most effective method is to inject an artificially generated transit to the photometric data, obtained in Brno, and then analyse detectability of the exoplanet by proper software. The exoplanets with relative transit depth of 2%, 1% and 0,57% were selected for this simulation. Detectability of the transit can be affected by the brightness of the star, the colour of the star depending on the changing altitude and the gradient of the chip's illumination caused by the Moon or by light pollution. Thus, dependence on the brightness, colour and distance of the stars is tested by a magnitude, colour and distance test during 3 different nights. The open star cluster M34 was chosen for photometry measurements, due to the diversity of the stars, their suitable distance from each other, and high culmination during the observations. Measurements took place at the Masaryk Universty Observatory by using telescope of diameter 0.6 metre and exposure time of 20 seconds in the $R$ filter. Our analysis shows that an exoplanet with a relative transit depth of 2% is detectable at all the selected stars (9 mag – 13.6 mag) during each of the three nights. An exoplanet with a relative transit depth of 1% has the widest transit of the selected exoplanets (0.11 days), which made it more difficult to detect, especially during nights with increased scatter in the data caused by clouds. The last of the exoplanets with a relative transit depth of 0.57% was best detectable during night 3, due to the best observation conditions. From the obtained results, we can assume that the detectability of transit is most affected by the signal-to-noise ratio, which depends on seeing and observation conditions, especially constancy of wind speed and atmospheric pressure.

## Poďakovanie

Na tomto mieste by som chcel poďakovať svojemu vedúcemu Mgr. Marekovi Skarkovi, Ph.D. za usmerňovanie počas celej práce, za cenné rady, výdrž, ochotu a ústretový prístup pri konzultáciách. Takisto by som chcel poďakovať aj Mgr. Václavovi Glosovi za pomoc, podporu a ochotu pri písaní tejto práce.

## Čestné prohlášení

Prehlasujem, že som svoju bakalársku prácu vypracoval samostatne pod vedením vedúceho práce s využitím informačných zdrojov, ktoré sú v práci citované.

Brno 17. 8. 2020

Podpis autora

MASARYKOVA UNIVERZITA
PŘÍRODOVĚDECKÁ FAKULTA
KOTLÁŘSKÁ 2, 611 37 BRNO
IČ: 00216224
DIČ: CZ00216224

# ZADÁNÍ BAKALÁŘSKÉ PRÁCE

Akademický rok: 2019/2020

| | |
|---|---|
| **Ústav:** | Přírodovědecká fakulta |
| **Student:** | Marko Mesarč |
| **Program:** | Fyzika |
| **Obor:** | Astrofyzika |

Ředitel *ústavu* PřF MU Vám ve smyslu Studijního a zkušebního řádu MU určuje bakalářskou práci s názvem:

| | |
|---|---|
| **Název práce:** | Pozorovatelnost exoplanet v městských podmínkách |
| **Název práce anglicky:** | Observability of exoplanets in the city environment |
| **Jazyk závěrečné práce:** | angličtina |

**Oficiální zadání:**
Exoplanety je dnes možné pozorovat metodou tranzitu relativně snadno i s malými dalekohledy. Přirozeně však existují limity dané pozorovacím prostředím a použitými přístroji. Cílem práce je zjistit nejmenší detekovatelný pokles jasnosti v závislosti na nastavení přístrojů Masarykovy univerzity a vlastnostech hvězdy v podmínkách městského prostředí v Brně.

| | |
|---|---|
| **Vedoucí práce:** | Mgr. Marek Skarka, Ph.D. |
| **Konzultant:** | RNDr. Jan Janík, Ph.D. |
| **Datum zadání práce:** | 5. 12. 2018 |
| **V Brně dne:** | 13. 8. 2020 |

# *Contents*

# *Introduction*

Since 1995, when the first exoplanet was discovered, 25 years have passed. Ever since then, every year, we detect tens of new extra-solar planets by modern ground telescopes and space telescopes. Up to August 16, 2020, 4201 planets have been confirmed as extra-solar planets, and another 5481 are catalogued as potential candidates (NASA.gov, 2020).

In my thesis, I focus on the detectability of exoplanets in the city environment. People who live in the city know that light pollution is one of the main factors leading to worsened conditions for observation. The bigger the city, the more light pollution there is. Astronomers and scientists who are interested in research related to photometry, know that light pollution is not the only factor that affects observation. Factors such as phases of the Moon, light scattering, colour extinction, humidity, cloudiness, used telescope and detector belong into this category. All of these factors were considered when photometry was taken during three different nights. I selected open star cluster M34 for photometry measurements. Measurements were taken at the Masaryk University Observatory, which is located at Kraví hora, Brno.

The thesis is structured into five sections in terms of content. In section 2, the history of the view of “other worlds” is discussed, the term exoplanet is defined and the formation of planetary systems is described. The methods with principles of searching extra-solar planets are mentioned at the end of the section.

The introduction of section 3 focuses on how the CCD chips work and some features of CCD are mentioned, too. The next part of this section is dedicated to the basic principles of the CCD image correction and the photometry method used is explained. At the end of the section errors and factors that affect observation are discussed.

In the beginning of section 4 the three tests are described and it is clarified why they had to be done. Then it is explained why an M34 open star cluster was chosen for photometry measurements and some facts about clusters are mentioned, too. The last parts of section 4 are dedicated to the software that was used to process data.

The last two parts of my thesis, section 5 and section 6, deal with the results of my work. There are results of all three tests and the impact of observation conditions are also discussed. Last but not least, the most important are the results of the magnitude range of the stars at which transit with different depth can be detected.

*“We began as wanderers, and we are wanderers still. We have lingered long enough on the shores of the cosmic ocean. We are ready at last to set sail for the stars.”*

Carl Sagan, Cosmos

## 2.1 A brief history of the search for exoplanets

"Are we alone in the whole Universe?" This is the most debatable question humanity can ask. Since we know that those "white dots" in the night sky are stars like the Sun, this question is understandable. Our Galaxy has approximately 100,000 ly in diameter (Rix & Bovy, 2013), contains between 100-400 billion stars (NASA.org, 2020) and at least 100 billion planets (Cassan et al., 2012). When we think about those huge numbers, there is a chance that somewhere in the Milky Way Galaxy Earth-like planets hosting life exist.

Since Galileo Galilei pointed a telescope at the night sky for the first time ever and discovered Jupiter's four moons, a lot of time has passed. At that time, the construction of a device that could detect other worlds was impossible. Today, we are at a different technological level. We are building telescopes not only on the Earth's surface but also in space. Even though the chance of detecting extra-solar planets is low, telescopes are capable of overcoming this challenge. The category of space devices that might detect transits includes, for example, *Kepler*, *TESS* and also the most modern James Webb Telescope, which will be hopefully launched on October 31, 2021. Nevertheless, when have we started thinking about the "other worlds"?

These thoughts, questions and ideas started appearing in the 4$^{\text{th}}$ century B.C., articulated by philosophers like Aristotle and Epicurus. First of the mentioned philosophers had an idea that our planet is so remarkable that it must be in the centre of the universe. Epicurus believed that our planet is one of many that are either similar to or different from the Earth. Now we know that he was right, however in that time, Aristotle had a great authority, so, unfortunately, opinions on the existence of other worlds were disregarded (hvezdy.cz, 2020).

It took more than 2000 years until the idea of extra-solar planets was taken more seriously. Everything started with the Polish astronomer Nikolai Copernicus. In the 16$^{\text{th}}$ century, he published his heliocentric theory and put our Sun, instead of the Earth, into the centre of the Solar system and the universe. Several years later, Italian philosopher Giordano Bruno took Copernicus status about the Sun and claimed that even the Sun is not in the middle of the universe. In addition, he suggested that our closest star is one of the many in the universe. He was sure that distant stars were similar to our Sun, therefore, harboured planets of their own (hvezdy.cz, 2020). This view was also supported by Isaac Newton (Newton & Cotes, 1713).

Humanity had to wait until we technologically progressed to a higher level. Each century has brought new technologies that help us with the detection of exoplanets.

## 2.2 Definition

Our Solar System is one among many in the Galaxy. Since the 20$^{\text{th}}$ century, we have taken for granted that most of them have their own planetary systems as we can infer from the number of exoplanets that have been discovered so far. A planet that is found beyond our Solar System and orbits a star is called an *exoplanet*, or *extra-solar planet*. This is the first reasonable formulation based on what we have observed. However, there are also exoplanets that do not orbit a star, but orbit galactic centre directly - we call them rogue or nomad planets (Lloyd, R., 2001). Based on observations, one study estimates that there are two

Jupiter-mass nomad planets for every star in the Milky Way (Sumi et al., 2011). In 2003, researchers confirmed the existence of the first circumbinary exoplanet (Thorsett et al., 1993), planet which orbits two stars. Because nomad and circumbinary planets do not orbit their parent stars, the first definition of an extra-solar planet needs to be modified.

When a new exoplanet is discovered and astronomers calculate its parameters, the decisive parameter is the mass. In the universe, there are objects, such as brown dwarfs which cannot be classified as planets. These objects have not enough mass to sustain the nuclear fusion of hydrogen in their cores. Despite this, their mass is sufficient for the fusion of deuterium or lithium, but not for a long-term and so they are in a transitional space between planets and stars. They have a specific value of mass from 13 $M_{Jup}$ to 80 $M_{Jup}$ (Boss, 2001).

Therefore, the last option is to define an exoplanet by mass – *an exoplanet is a planet beyond our Solar System whose mass is lower than 13* $M_{\mathrm{Jup}}$.

## 2.3 Creation and where to search

Before stellar systems begin to form, an impulse is needed. It could be the result of passing star or a shock wave from a supernova. The result is a gravitational collapse at the center of the cloud, from which a star is later formed. Regarding planetary formation in stellar systems, scientists generally support – *the nebular hypothesis.* This hypothesis claims that planets were created by the accretion of microscopic particles of solid material and gas into a larger object in the protoplanetary disk – a rotating disk of dense gas and dust surrounding a young, newly formed star (D'Angelo & Bodenheimer, 2016). Furthermore, the hypothesis offers explanations for a variety of properties of the Solar System, including the nearby circular and coplanar orbits of the planets (Woolfson, 1993).

In distant parts of space, we observe giant molecular clouds (e.g., the Orion nebula, the Eta Carinae nebula), the beginnings of future stellar systems (Figure 2.1). Based on these observations, we are able to tell how our planetary system developed, and then we can predict the evolution of observed systems. It is theorized that planets are formed within a few to tens of millions of years after their star formation (Yin et al., 2002).

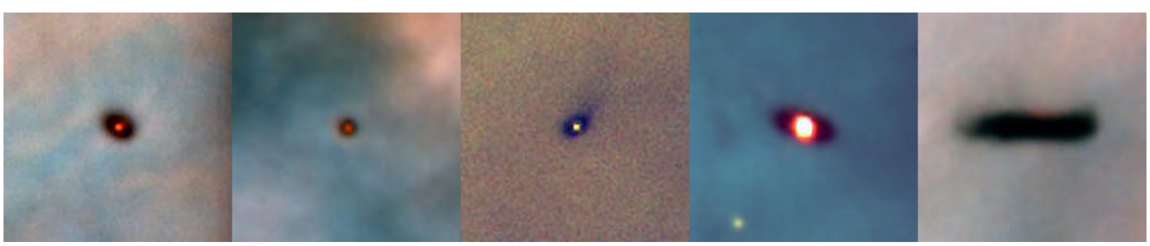

Figure 2.1: Image showing protoplanetary disks in visible light around young stars that were discovered by *Hubble Space Telescope* in the Orion Nebula located 1500 light-years away. The image had been created by combining three filters: blue OIII – 502 nm, green H-alpha – 656 nm and red NII – 658 nm (credit: Mark McCaughrean – Max-Planck-Institute for Astronomy, C. Robert O'Dell – Rice University and NASA/ESA, 2020).

At the beginning of 2020, there are more than 4100 confirmed exoplanets and more than 5000 candidates (NASA.gov, 2020). The main goal of astronomers is not only to find planetary systems but, more importantly, to find those that are suitable for life, where oxygen, water, appropriate temperature and other conditions are fulfilled. These parameters depend mostly on the size of the semi-major axis of the exoplanet's orbit and radiative flux of the host star. The region that has the appropriate distance from the parent star, also defined as a region where the water will remain in all three states, is called a *habiTable zone*.

Life itself needs millions of years to evolve – a process that begins from prosperous conditions for life to tiny unicellular organisms or intelligent minded beings. Certainly, life cannot evolve in stellar systems whose parent stars are too massive. The more massive the star, the shorter its life will be. This applies to the stars of spectral type O, B, A, F. Associated with spectral types and lifetimes of the stars is the *main sequence* – the area on the Hertzsprung-Russell diagram, where stars spend most of their lives by fusion of the hydrogen in their cores. For the above-mentioned stars (O, B, A, F) the lifespan spent on this area is too short to provide enough time for development of life, compared to the Sun. When these stars leave the main sequence they inflate and become red giants – a type of star that will destroy life rather than support it. Less massive stars, also known as M-dwarfs, are problematic as well. They have low luminosity, thus, a habitable zone must be closer to the star for it to provide enough thermal energy needed in case of occurrence of life on the planet. However, the stellar activity of these stars combined with their flaring and very strong magnetic fields can have devastating effects on life development.

When we want to find life, we should turn our attention to stars which are at least comparable to our Sun (G-type star) in terms of brightness, stellar activity, mass and, thus, lifespan on the main sequence. Research shows that orange dwarfs may host habitable planets. Astronomers started calling them *Goldilocks stars*, also known as K-type stars. They were named after the project "GoldiloKs" which is focused on measurements of the age, rotation rate, and the X-ray and far-infrared outputs of a sample of cool G and warmer K stars. People of that project use NASA's *Hubble Space Telescope*, NASA's *Chandra X-ray Observatory*, and the European Space Agency's *XMM-Newton satellite*. It turns out that the planets of K-type stars, especially the warmer ones, are of interest in the search for extraterrestrial life. It is mainly because they emit less ultraviolet radiation than G-type stars (can damage DNA), and they are stable on the main sequence for a very long time (15 to 45 billion years), so potential life has enough time to prosper (NASA.gov, 2020).

## 2.4 Methods of discovering exoplanets

The sizes of planets are mostly very small compared to the sizes of the parent stars, thus, astrophysicists had to make up mechanisms, or methods on how to prove that exoplanet is surely there. In the 21$^{\text{th}}$ century, there are 5 methods which are frequently used. Four of them are quite successful, except for one – astrometric method. Only one planet has been discovered using this method *DENIS-P* J082303.1-491201 b in constellation Vela, using FORS2 camera at the VLT located at the Paranal Observatory (Sahlmann et al., 2013). Thus, in the next sub subchapters, I would rather focus on methods that have already worked in more than one case.

### 2.4.1 Direct imaging

Planets are mostly faint light sources compared to the stars and therefore direct observation of planets seems impossible. First we have to deal with the excess light coming from the parent star. It can be ensured by observing at longer wavelengths, using light blockers and even interferometry.

The observation in longer wavelengths of the spectrum utilizes the Wien's displacement law – the cooler the object, the longer wavelengths of maximum radiated energy. Planets are colder in comparison with stars and that is why they radiate the most in the infrared spectrum. When observation is taking place from a ground-based telescope, it is necessary to count with atmospheric turbulences – seeing. This distortion of the atmosphere can be corrected by adaptive optics (Babcock, 1953). It compensates seeing by providing a reverse deformation of the mirror that uses a fast-response system. With the aid of the adaptive optics, such images of planetary systems as shown in the Figure 2.2 can be taken.

Using direct imaging method, exoplanets are detected by coronography – also used for observing the Sun's corona. The device is placed inside the telescope to block light from the parent star before it reaches a detector. The way, which is probably our future of direct imaging, is interferometry. The apparatus consists of two telescopes, but in one of them is an inserted system of mirrors – delay line. Appropriate delay setting will cause destructive interference and star disappears from the image. Thus, the same principle we can use to constructive interference and light of the planet will intensify (astrin.planetarium, 2020).

The first planet discovered by using direct imaging was *Beta Pictoris* b in 2008 (Lagrange et al., 2009). To the day of 16$^{\text{th}}$ August 2020, 50 out of 4201 exoplanets were discovered using direct imaging method (NASA.gov, 2020).

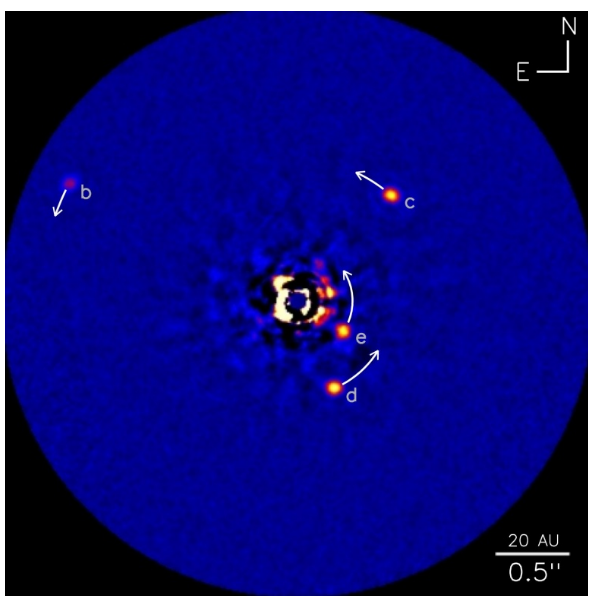


Figure 2.2: Chart showing four planets in the HD 8799 system which is located 129 light-years away from the Earth in the constellation of Pegasus. The image was taken by Keck Observatory's near-infrared adaptive optics (edited, credit: Marois et al., 2008).

### 2.4.2 Gravitational microlensing

Albert Einstein, in accordance with his Theory of General Relativity (Einstein, 1936), claimed, that gravity of massive objects bends light. The more massive the object is, the more it curves the direction of light. These objects can be stars, black holes or whole galaxies. In order to detect a planet by this method a distant star and a foreground-passing star is needed. Both of them need to be on the line of sight. The gravitational field of the foreground star warps space and creates a gravitational lens which is magnifying the light of a distant background star. In case that a planet is orbiting a passing star, it may appear as a short-term brightening on the light curve as the Figure 2.3 shows.

A great advantage of this method compared to the others is that a planet can be detected thousands of light-years away. Microlensing is also very sensitive to detect low-mass planets in wider orbits around Sun-like stars. That is why this makes gravitational microlensing a great method for finding Earth-like planets. The main disadvantage of gravitational microlensing is that we never know when or where this phenomenon occurs. Astronomers have to watch large parts of the sky over a long period of time. Unfortunately, a chance of occurrence will not repeat, thus, micro-lensing exoplanet cannot be studied anymore.

Sky surveys based on the research collaborations using the gravitational microlensing method are OGLE, MOA and SuperMACHO. The first success was made in 2003 by both OGLE and MOA using microlensing to detect exoplanet and it was OGLE 2003–BLG–235/MOA 2003-BLG-53 (Bond et al., 2004). To the day of 16$^{th}$ August 2020, 96 out of 4201 already known exoplanets were discovered using gravitational microlensing method (NASA.gov, 2020).

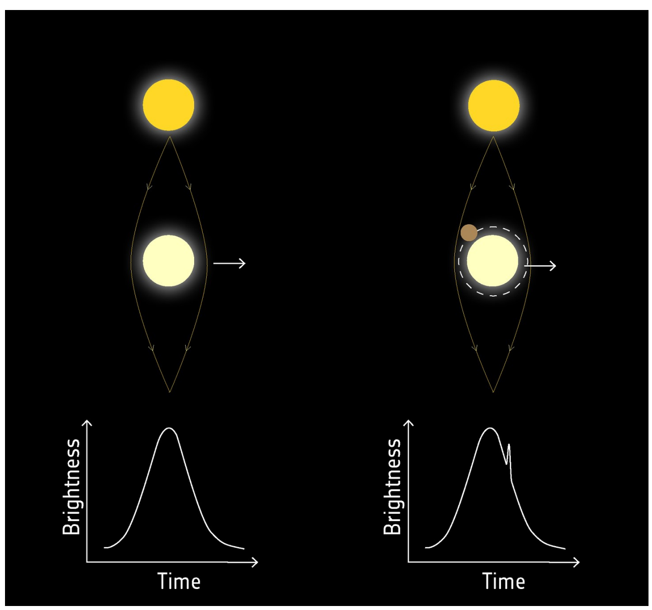


Figure 2.3: Chart showing how gravitational field bends space to create a gravitational lens that magnifies light. Deviation due to planet's mass will create a detecTable change in brightness which manifests as a small bulge - it is shown on the right-hand side of the chart (edited, credit: ESA.int, 2020).

### 2.4.3 Measurement of radial velocity

A planet never orbits a star, more specific expression is that both of them are orbiting the common centre of mass. This leads to the periodical movements – one time is closer the star and the other time is closer an exoplanet to the Earth. Thus, when an extra-solar planet moves towards us, a star moves away and its spectral lines move to the red region of the spectrum. If an extra-solar planet moves away from us, a star gets closer, so its spectral lines move to the blue region of the spectrum as the Figure 2.4 shows. That is called a Doppler's effect.

If we plot the shift of spectral lines as a function of time, we get a periodic curve from which we can estimate the eccentricity of the planet's orbit, its orbital period, the semi-major axis of the orbit and minimal mass of the planet.

Determination of the planet mass can be problematic because we do not know the exact inclination of its orbit towards the observer. Therefore, the calculated mass is only the bottom limit of the planetary mass. One of the main advantages of the radial velocity method is that we are able to detect even the Earth-like planets orbiting low-mass K-type and M-type stars – red dwarfs. Studies indicate that these stars are the most likely places to find terrestrial planets with water on their surface (Alibert & Benz, 2017).

There are hundreds of observatories, which use radial velocity method to detect the exoplanets, for example ESO in La Silla Observatory in Chile, Haute-Provence Observatory in France or even in Ondřejov in the Czech Republic and Stará Lesná in the Slovak Republic. The first planet orbiting a main-sequence star was detected using this method in 1995 – 51 Pegasi b (Mayor & Queloz, 1995). To the day of 16$^{\text{th}}$ August 2020, 810 out of 4201 exoplanets were discovered using radial velocity method (NASA.gov, 2020).

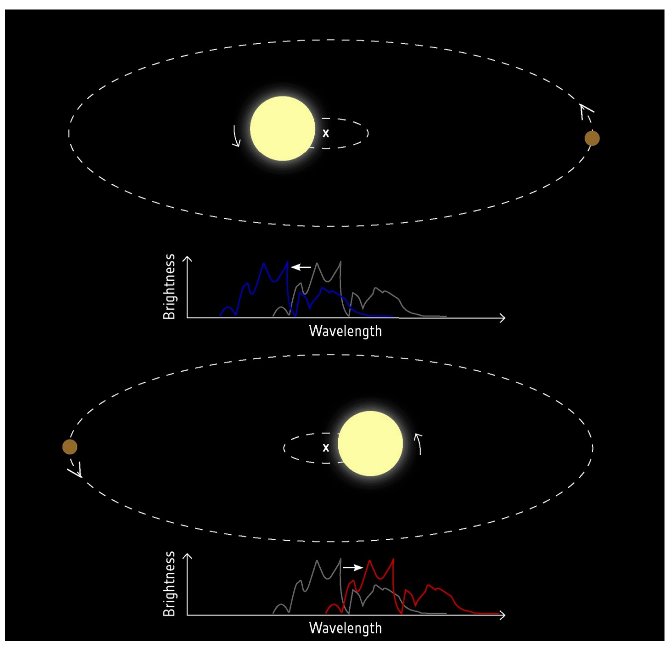


Figure 2.4: Chart showing how the spectral lines move depending on how exoplanet deflects the star (edited, credit: ESA.int, 2020).

### 2.4.4 Transit method

Using the transit method, also called transit photometry method, most of the extra-solar planets were discovered. This method is used to measure the amount of light from distant stars to detect exoplanets in stellar systems. As a default apparatus astronomers use the CCD chip which is an important part of space telescopes or ground-based telescopes that use transit photometry to detect extra-solar planets (how CCD works is described in section 3). The method of transit photometry is most often combined with the method of radial velocity. We are able to obtain radius, the inclination and also an orbital period of the distant planet by analysing the results of the transit method and we can determine at least the lower limit of planet mass by radial velocity method. Hence, we are capable of figuring out missing parameters by using these values and then find out pretty much any information about the stellar system. To simplify the situation, in the next models we will assume a circular orbit of the planet and constant brightness from the entire star's surface.

If the planet passes in front of its parent star, this event is called a *transit*, then the visual brightness of the star drops by a small amount – depending on the ratio of the sizes of the planet and the star. The relative decrease of the star's brightness in such a transiting planet is given by

$$\Delta F \approx \left(\frac{R_{\mathrm{p}}}{R_{\mathrm{s}}}\right)^2, \tag{2.1}$$

where $\Delta F$ is the relative flux of the star, $R_{\mathrm{p}}$ is the radius of the planet and $R_{\mathrm{s}}$ is the radius of the star. The larger the planet, the more light of the star is blocked. In the assumption that somewhere in the space a distant observer observes our Solar System, he would have measured that the biggest planet Jupiter blocks 1% of the Sun's light but the Earth blocks only 0.008% of the Sun's light. When a transit-like event is observed, two indicators can prove that it is really caused by a planet. First indicator is a periodical dimming. The second is if the brightness is reduced by the same amount each period. When those indicators are present, there is a high chance that a planet is present. These changes caused by a potential planet are plotted in a graph known as *light curve* which shows the brightness of an object, in our case a star, as an function of time.

Stars with their extra-solar planets are located in different distances and different directions from the Earth. Therefore, the observer must be in a favourable position to detect such a decrease in the star's brightness. The right position for a transit's occurrence is that the orbital plane of the exoplanet crosses the plane of the observer – a view from the side. This means that detectable transit occurs as long as the following formula applies

$$a \cdot \cos i \leq R_{\mathrm{s}} + R_{\mathrm{p}}, \tag{2.2}$$

where $a$ is the semi-major axis and $i$ is the *orbital inclination* – angle between the plane of the orbit relative to the plane perpendicular to the line of sight from the Earth to the planet (Figure 2.5). The minimum inclination required to detect the planet's passage in front of the star can be derived from the formula 2.2 as

$$i_{\mathrm{min}} = \arccos\left(\frac{R_{\mathrm{s}} + R_{\mathrm{p}}}{a}\right). \tag{2.3}$$

The primary transit is not the only useful thing, from which one can be determine a

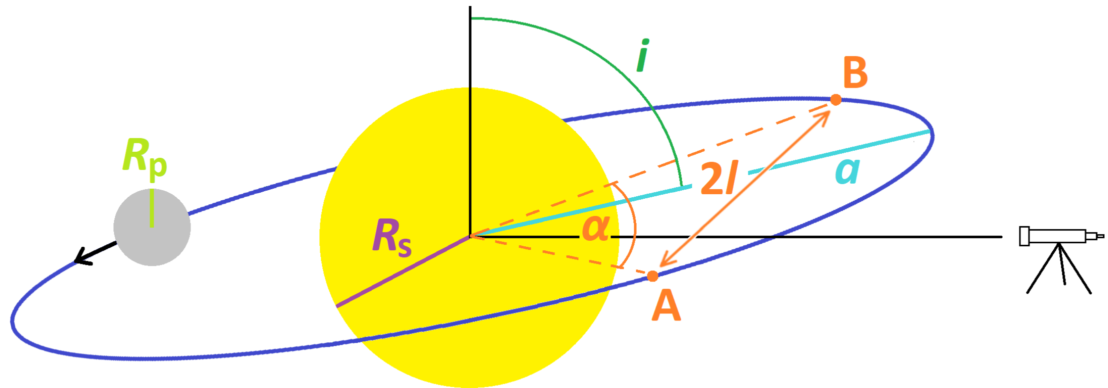


Figure 2.5: The orbital geometry of transiting extra-solar planet.

composition of planet's atmosphere. Even the planet's passage behind its parent star, a *secondary eclipse*, can be used for some purposes. Astronomers can find the temperature of the planet by a simple measurement of the photometric intensity of the parent star and then subtracting it from measurement before the secondary eclipse.

For transiting exoplanets, an *impact parameter* – $b$ is introduced. It is the minimal projected distance between the centre of the stellar disc and the centre of the planetary disc at the conjunction (Figure 2.6). An impact parameter is a dimensionless quantity and can be expressed as

$$b \cdot R_\mathrm{s} = a \cdot \cos i. \tag{2.4}$$

If $b = 0$ then the transit duration is the longest, because the planet passes through the whole diameter of the star (edge-on orbit), Figure 2.7. On the contrary, if $b \neq 0$ transit duration is shorter because the planet travels the distance given by the equation 2.4 and as is shown in the Figure 2.6 and the Figure 2.7 (tilted orbit).

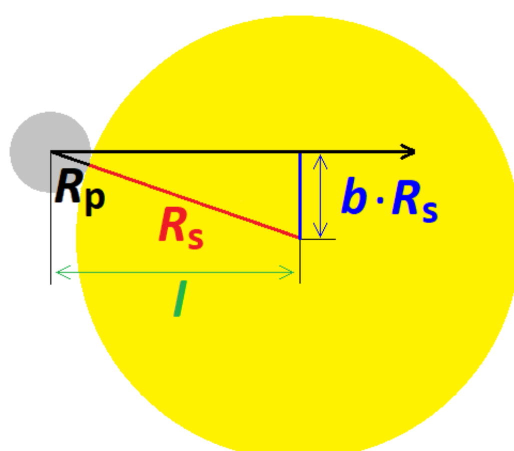


Figure 2.6: Star-planet geometry – tilted orbit.

When transit occurs, naturally, it is good to know how long it will last in case we want to detect it using a ground-based telescope. The duration of the planet's transit in front of

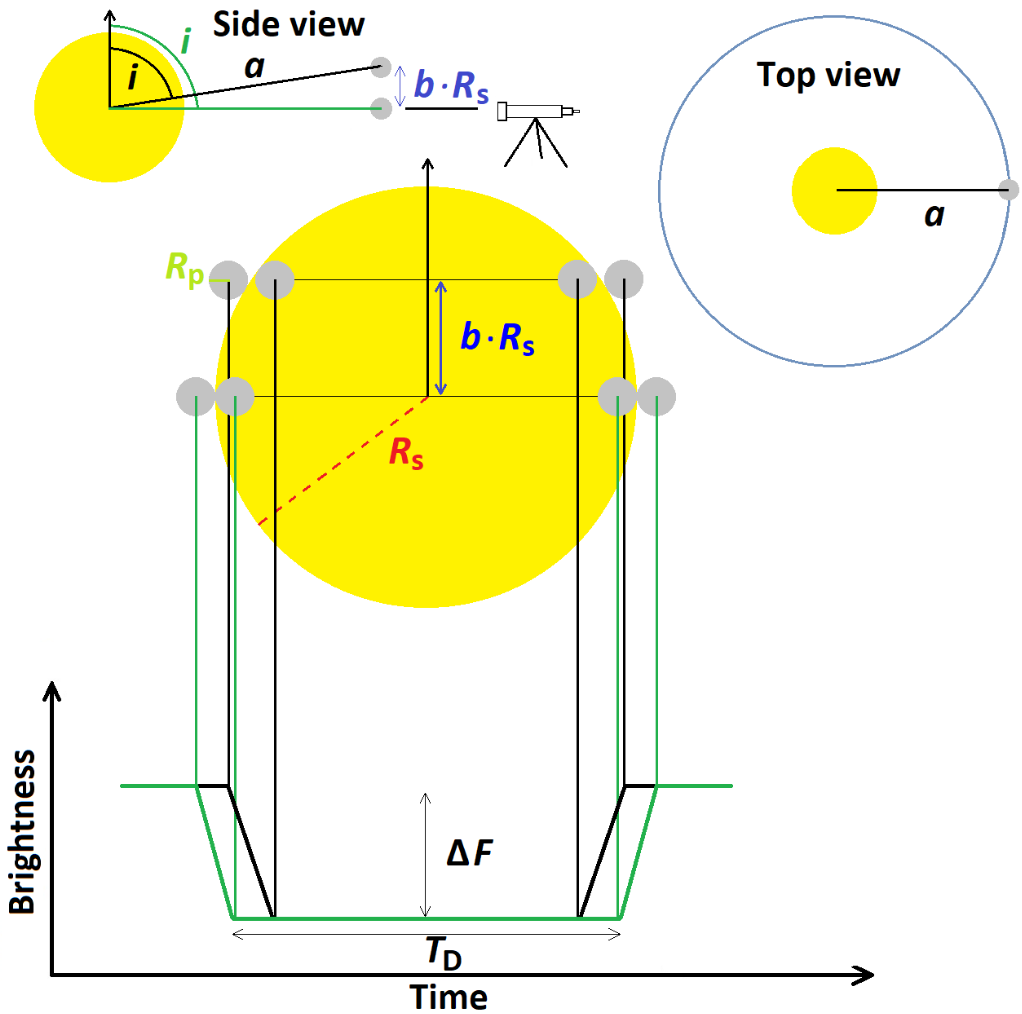


Figure 2.7: Chart showing how the decrease of the brightness of the stars looks like by two transiting planets with different inclinations, black colour is for tilted orbit – ($0° < i < 90°$), ($b \neq 0$) and green colour is for edge-on orbit – ($i = 90°$), ($b = 0$).

its parent star is implied by the geometry shown in the Figure 2.6 and by using Pythagoras's theorem

$$2l = 2\sqrt{(R_\mathrm{s} + R_\mathrm{p})^2 - (b \cdot R_\mathrm{s})^2}, \tag{2.5}$$

where $l$ indicates the length that the exoplanet has to travel in front of the stellar disc. The next step to a better understanding of the situation can be indicated from the Figure 2.5, where extra-solar planet passes through the points from A – the beginning to B – the end of the transit. An exoplanet creates an angle $\alpha$ (Figure 2.5) with arc distance $\alpha \cdot a$ as regards to the centre of the parent star. For a triangle formed by the centre of the star and points A, B follows

$$\sin\left(\frac{\alpha}{2}\right) = \frac{l}{a}. \tag{2.6}$$

By combining the equations 2.5 and 2.6 we get a formula to calculate transit duration $T_\mathrm{d}$

$$T_\mathrm{d} = P \cdot \frac{\alpha}{2\pi} \sim \frac{P}{\pi} \cdot \arcsin\left(\frac{l}{a}\right) \sim \frac{P}{\pi} \cdot \arcsin\left(\frac{\sqrt{(R_\mathrm{s}+R_\mathrm{p})^2 - (b \cdot R_\mathrm{s})^2}}{a}\right), \tag{2.7}$$

where $P$ is orbital period of the extra-solar planet. A distant observer who will be able to observe our Solar System with $i = 90°$, would have measured the duration of transits from 8 hours for Mercury to 71 hours for Neptune. From the equation 2.7, the formula for the true inclination can be derived as

$$i = \arccos\sqrt{\frac{(R_\mathrm{s}+R_\mathrm{p})^2}{a^2} - \sin^2\frac{\pi \cdot T_\mathrm{d}}{P}}, \tag{2.8}$$

In case the planet orbits the parent star periodically without major changes, $P$ can be estimated from the light curve. From the already stated orbital period we are able to calculate an $a$ by a simple modification of the third Kepler's law

$$a = \sqrt[3]{\frac{P^2 \cdot G \cdot (M_\mathrm{s}+M_\mathrm{p})}{4\pi^2}} \sim P^{\frac{2}{3}}, \tag{2.9}$$

where G is gravitational constant, $M_\mathrm{s}$ and $M_\mathrm{p}$ are masses of star and planet.

In real life, the light curve does not have such a distinct minimum as in the Figure 2.7. More accurate models, which work with measured data or create hypothetical simulations of transit curves, consider, that a star is not a uniformly radiating disk, but rather exhibits the signs of *limb darkening*. It is a property of each star based on an existing temperature gradient in the photosphere. Looking to the centre of a stellar disc, we see deeper and warmer layers of the photosphere. While at the edge we see photosphere at a certain edge, with its higher layers which are colder. Thus, the centre is hotter and therefore brighter than the edges as the Figure 2.8 shows. Limb darkening causes that light curve has a typical U-shape compared with straight shape when limb darkening is not taken into account. This is shown in the Figure 2.9 which represents dependency of transits depth on the different ratio of the diameter between the planet and star ($R_\mathrm{p}/R_\mathrm{s}$), and the Figure 2.10 which shows the dependency of transits depth on inclination.

The transit photometry method is very successful despite its flaws. One of the disadvantages is that the planetary transit occurs only when the formula 2.3 applies. In other cases we are not able to detect dips in star's brightness caused by a planet. Another issue is that we do not know when the transit is going to happen. To increase the chance of detecting exoplanetary transit, it is good to monitor continuously thousands of stars at the same time. Therefore, it is better when extra-solar planets have a much shorter orbital periods than the Earth, because the transit occurs many times during long monitoring. Luckily, many detected exoplanets have orbital periods less than a few days some even hours. That is the reason why many periodic dips are visible on the light curve and that it can be a good sign of a planet. The transit method also tends to produce false positives. The smallest stars can have similar diameters as giant planets. Thus, in that way measurement of radial velocity needs to be provided to confirm that the diameter and/or mass of those objects are small enough to be considered as planets.

Figure 2.8: Image showing limb darkening of the Sun. On the right-hand side of the Sun, sunspots are visible. The image was captured on 9$^{\text{th}}$ of July 2017 using the method of indirect observation of the Sun by projection.

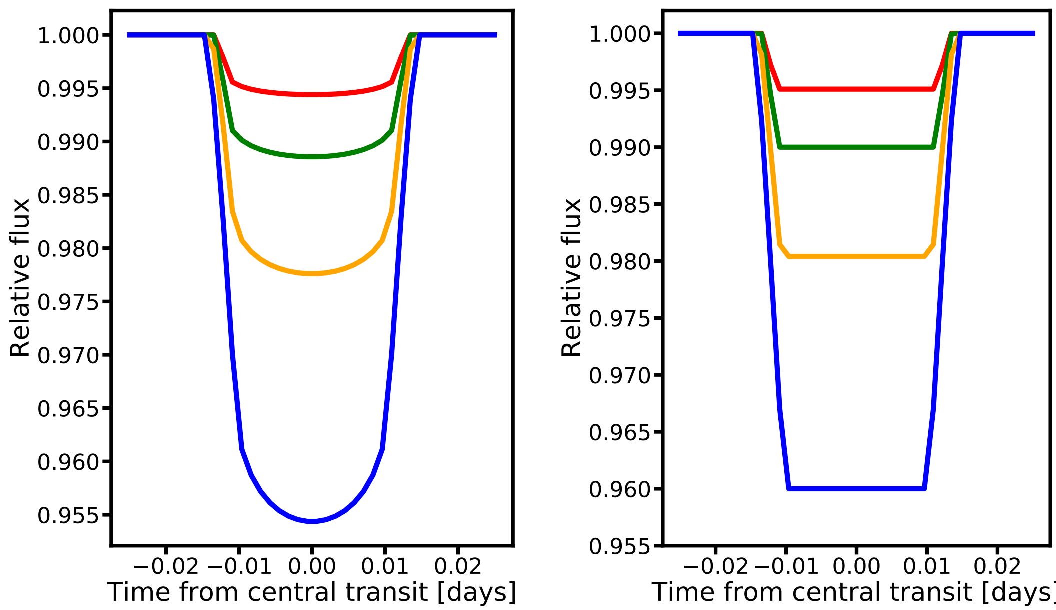


Figure 2.9: Plots showing how the light curves look like when we consider limb darkening – on the left-hand panel and when not – right-hand panel. Four transiting planets are shown in both of graphs with the same $i = 90°$, but different ratio of $R_{\mathrm{p}}/R_{\mathrm{s}}$. Blue – 0.2, orange – 0.14, green – 0.1, red – 0.07.

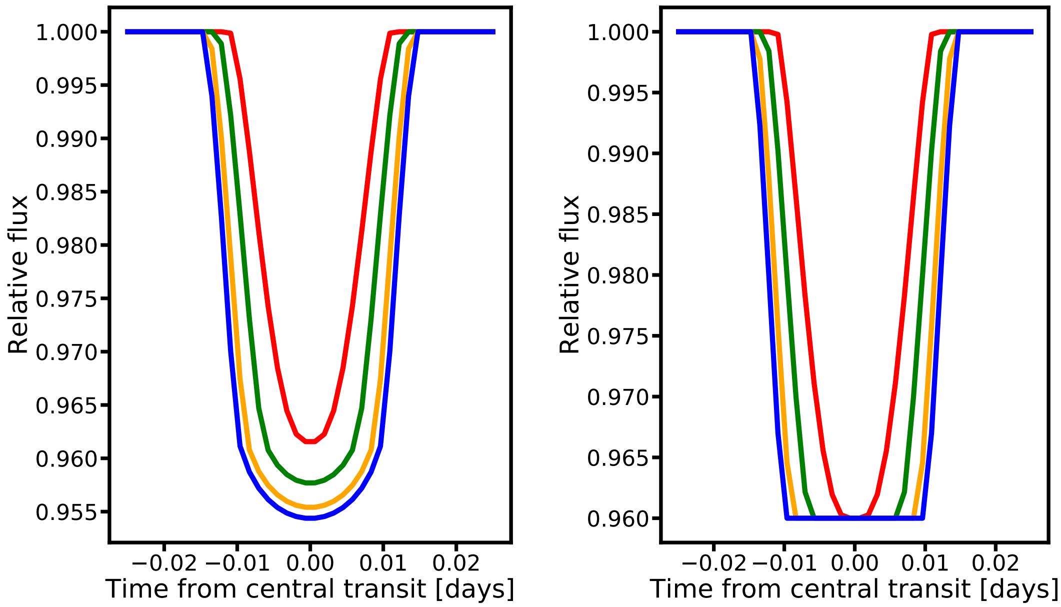


Figure 2.10: Plots showing how the light curves look like with varying inclination respect to when we consider limb darkening – on the left-hand panel and when not – right-hand panel. Four transiting planets are shown in both of graphs with the same $R_{\mathrm{p}}/R_{\mathrm{s}} = 0.2$, but different $i$, $b$. Blue – 90° ($b = 0$), orange – 89.4° ($b = 0.01$), green – 89° ($b = 0.02$), red – 88.7° ($b = 1.3$).

The NASA's first space telescope which was designed to detect Earth-sized planets and made the transit method famous is *Kepler*. It was focused on stars in the constellations Cygnus-Lyra and later extended to the ecliptic. On 18$^{\mathrm{th}}$ April 2018, it was joined by *TESS* which gradually scans all parts of the sky looking for extra-solar planets and selecting targets for detailed study by the *James Webb Space Telescope (JWST)* – scheduled to be launched in 2021. The research focused on the exoplanets discovered by using the transit method can continue to study their atmospheres. For this a technique so called – *transit spectroscopy* is used, and by using it, we can study structure and composition of the atmospheres of transiting exoplanets. The state-of-the-art space-based *JWST*, will have such a technology and will provide more of an accurate research of the chemical composition of exoatmospheres.

Likewise, the European Space Agency (ESA) has its space missions. The *Convection Rotation and Transits* (*CoRoT*) was the first-ever space mission dedicated to rocky extra-solar planets. Each of 150 days *CoRoT* moved to a new field and began to observe again. Its greatest discovery was CoRoT-7b (Léger et al., 2009), the first transiting terrestrial planet. In December 2019, *Characterising Exoplanet Satellite* (*Cheops*) has started its mission focused on the bright, nearby stars that are already known to host extra-solar planets. *Cheops* is focused on exoplanets from the super-Earth to Neptune size range with the aim to make high-precision observations to set the bulk density of the exoplanets. Another planned space telescope is *PLATO*, whose launch is expected in 2026 to the Earth-Sun

L2 Lagrangian point. The main goals of the mission are to search for new exoplanetary systems and to discover, and characterize rocky extra-solar planets in the habitable zone around sun-like stars, even red dwarf stars.

Also, multiple ground-based telescopes are involved to searching for extra-solar planets. They often have several cameras to scan the widest possible field of view, so that they capture as many stars as possible. Lenses do not have large diameters, often only a few centimetres. Ground-based telescopes need as good observable conditions as possible for measurements. For that reason, these telescopes are located in higher places to minimize atmospheric extinction, and that can even avoid light pollution from the cities. To this category KELT, SuperWASP, TRAPPIST or OGLE belong to. To the day of 16$^{\text{th}}$ August 2020, 3191 out of 4201 already known planets were discovered by using transit photometry method (NASA.gov, 2020).

# CCD photometry

## 3.1 Principles and features of CCD

A charged-coupled device (CCD) was invented in 1969 by Williard Boyle and George E. Smith of the Bell Laboratory (Boyle & Smith, 1970). Both of them were awarded a Nobel prize for physics in 2009.

CCD chip is an electronic component used for capturing image information (Figure 3.1). Originally it was invented as a memory device, but later it was discovered that it has a great quality of light detection. Nowadays, CCD is a common component of scanners, cameras, and also of scientific instruments like telescopes.

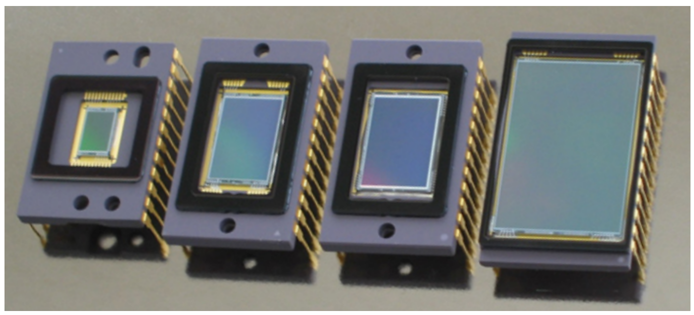

Figure 3.1: Kodak Full Frame CCDs: KAF-0402ME, KAF-1603ME, KAF-3200ME and KAF-6303E (edited, credit: gxccd.com, 2020).

A charged-coupled device consists of tiny elements – pixels, which create an elementary display unit. They are of the size of a couple of micrometres, and they are arranged into vertical and horizontal directions – rows and columns. The more pixels, the higher resolution the chip has. In terms of quantum mechanics, each pixel is, in fact, a potential well in which the silicon layer is located. As many light-sensitive components, CCD uses a physical phenomenon called the *photoeffect*. When a photon interacts with the atom, it can provide enough energy to get an atom to an ionized state. That energy is characterized by

$$E = h \cdot f, \tag{3.1}$$

where $h$ is a Plank constant and $f$ is a radiation frequency. In other words, during the exposure, incoming photons are absorbed by the chip's silicon atoms and because of the photoelectric effect, give rise to free electrons.

An important feature of a CCD is the ability to accumulate light – the longer a chip is exposed, the more electrons are accumulated. These electrons are captured in the pixel's potential well by the electric field of the electrodes. When the exposure ends – the photons from distant object stop to interact with the silicon atoms – the electrons are read from each pixel. It happens in such a way that the electrodes by changing the voltage cause movement of collected electrons in each pixel – *electron pockets* from pixel to pixel. At the end of each row the so-called *output register* is located. It transports collected electron pockets in each pixel one by one to output amplifier and then to A/D converter, where electrons are counted and converted to an electrical signal. The Figure 3.2 schematically shows a simplified visualisation of the previous description. The obtained images – data

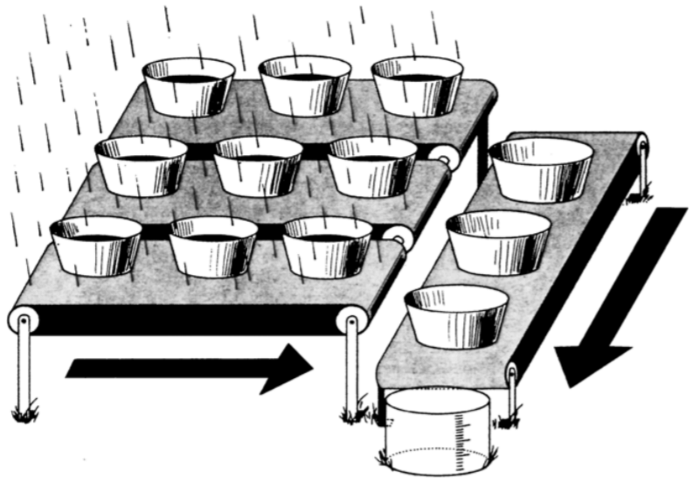

Figure 3.2: Image shows how a CCD's chip is read. In our analogy raindrops are incoming photons and fall into an array of buckets, which represent pixels. Water (the electrons) trapped in the buckets move to the end of the conveyor, and it is emptied into another bucket on a belt (output register). Then way carries to the metering station where the amount of water (the electrons) is measured (output amplifier), (credit: Howell, 2006).

sets – are saved in the *FITS* format (Flexible Image Transport System), which contains information about the captured electrical signal in each pixel. It is measured in units of *ADU* (Analog to Digital Unit). Besides that, all of the images have a header which contains information about e.g., date and time, what kind of optical filter was used, duration of the exposure and even the information about the temperature of the CCD's chip. The maximum value of the ADU is given by A/D converter, which can be 65,536 ADUs if 16-bit converter is used.

One of the basic features of CCD chips is the *quantum efficiency*. It has a statistical character and represents how many percent of the photons, which fall into the chip's area, are converted into a signal. The quantum efficiency of modern CCD cameras is on average about 75% – if 100 photons hit the chip, 75 of them will generate their own electron.

A *gain* belongs to other important features of the CCD chip. It expresses how many electrons captured by the CCD detector are needed to generate one ADU in the final image ($e^-$/ADU). The lower the gain, the higher the efficiency. Knowledge of gain is very important, firstly because various chips have sort of diverse gain and, thus, measured values are different. Secondly any quantity in the CCD image are measured only in units of ADU.

Chip quality is also characterized by the *dynamic range*. It denotes how many electrons generated by the photons the pixel is able to withhold. The maximum number of electrons that one pixel can retain is denoted by so-called *Full Well Capacity* (FWC). Exceeding FWC value causes saturation of the measured object. The dynamic range is limited firstly by the capacity of each pixel – maximum amount of electrons and secondly by the level of the pixel's own noise.

One of the most important features of astrophysical detectors is *linearity* and depends on which kind of A/D converter was used. It means that the output signal is proportional to the amount of incoming light on the whole of dynamic range. Unfortunately, chips are often not linear and that brings problems into to processing and calibration.

In astronomy, a feature called *binning* is often used in the majority of CCD cameras. It allows to combine charge (electrons) from several pixels together and work with greater amount of signal at the expense of camera resolution. Binning allows to get a better signal-to-noise ratio. The most used binning is 2x2 or 3x3, where instead of one pixel we get a collection area of four, respectively nine pixels.

Every object has different brightness that can change overnight, because of atmospheric extinction. When we make photometry of the object which is close to the saturation, a phenomenon called *blooming* is associated with that. It is the excess amount of produced electrons which flows into adjacent pixels and around the object parallel lines with different lengths are formed. Therefore, the correct exposure time had to be chosen. When it is selected too long, an excessive quantity of the photons fall on some pixels, and their capacity can overflow. This effect can be also eliminated by electrodes, which capture overflow electrons and lead them away – *anti-blooming* (Howell, 2006).

## 3.2 Basic correction of the CCD frames

Unwanted artefacts always appear in the image with photometric information. These artefacts reduce measurement accuracy, but fortunately, several methods exist, how we can eliminate them.

The CCD chip, as many electronic devices, heats up during use. Warming up causes thermal movement of the semiconductor's crystal grid and as a result, a spontaneous emission of electrons appears. This phenomenon is known as the *thermal noise*, also called the *dark current* and its amount depends on the exposure time. The higher the temperature, the greater the dark current. It means that thermal noise is also in the image. The noise of the CCD's sensor can be reduced by cooling with e.g., Peltier's cooler, a liquid nitrogen even dry ice. To eliminate thermal noise from the image it is necessary to get a so-called *dark image*. It is taken with the same temperature and exposure time as we did the image of the object, but the chip is not illuminated – shutter of the camera is closed. We get information only about the thermal noise this way. It is useful to take several dark frame images, make weighted median from them and create one *master dark frame* (Figure 3.3), which is subtracted from the raw image. Thereby, we get rid of thermal noise by using this procedure.

Other problems are caused by different sensitivity of the pixels and the non-uniform illumination of the chip, like a dirt on optical components. It is possible to get rid of all of these problems by getting an image of evenly illuminated area, the so-called *flat field*. Flat is usually taken with switched-off pointing clock drive, before the sunrise or after the sunset when the stars are not visible on the sky. A telescope is aimed at the opposite azimuth as the Sun had during the sunrise/sunset. Furthermore, the longer the exposure, the greater the differences in the brightness of the sky. However, when more photometric filters are used during the exposition, the flat field frame must be taken for all of the filters. This is necessary because each filter is slightly different, its position in the front of the camera may be different and there may also be dust grains on its surface. The flat field involves dark current noise, which can be removed by a dark frame. This dark frame is taken with the same exposure time and chip's temperature as flat field was taken. After subtraction, a weighted median is created from flats and then we create one *master flat field* (Figure 3.3).

Reading images from a charged-coupled device is connected with the so-called *read out noise*. Own electronic noise of CCD camera and process of reading electrons from the CCD chip belongs to this category. To subtract that kind of noise correction image, the *bias* is used. The bias image is exposed when a camera's shutter is closed and also in the shortest possible time that device can offer. The shortest time (ideal 0 sec.) guarantees that the frame does not contain dark current. However, bias is included in every single captured image and, therefore, by subtracting any two frames from each other, we actually remove the bias that is more or less the same for all frames.

Total calibration is given by

$$U = \frac{L - D}{F - D_{\mathrm{F}}}, \tag{3.2}$$

where $U$ is processed image of the object, $L$ is raw image of the object, $D$ is master dark frame, $F$ is master flat field and $D_{\mathrm{F}}$ is dark for flat.

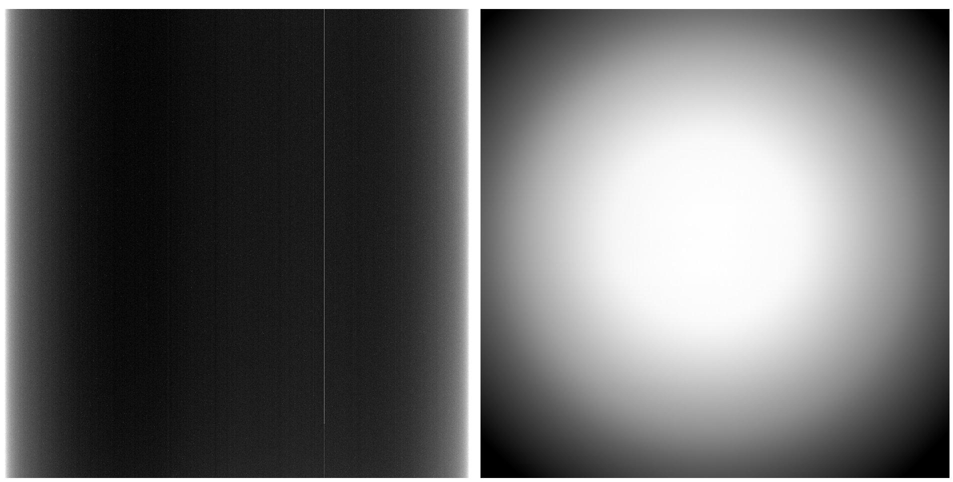

Figure 3.3: Images show how master dark (on the left-hand side) and master flat (on the right-hand side) in $R$ filter look like. In the master dark image, a white stripe is apparent, which is a sign of bad pixels in that column. Both of images were captured on 17$^{\mathrm{th}}$ September, 2019 at the Masaryk University Observatory.

## 3.3 Aperture differential photometry

After corrections of dark and flat frame, the image includes information about the signal from the object which we are interested in and fluctuation of background sky signal which must be subtracted. Most frequently the *aperture photometry* is used for this process, which sums the signal in pixels within a suitably selected aperture. As is seen in the Figure 3.4 not only the pixels which fit into its shape (blue colour) belong to the area bounded by the aperture, but also these, that fit only partially (turquoise colour). The aperture can be of any shape, but the most common profile used is square, ellipse or, as the Figure 3.4 shows, circle.

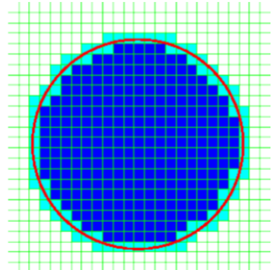

Figure 3.4: Scheme of aperture photometry with circle profile. Those pixels that belong to the aperture with their entire area are marked by blue colour. On the contrary, those pixels that belong to the area of aperture partially are marked by the turquoise colour (credit: Mighell, 1999).

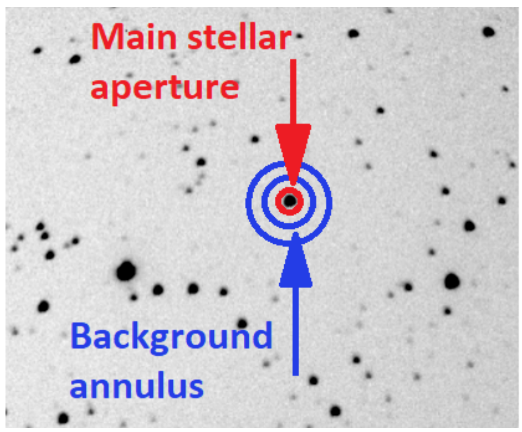


Figure 3.5: Aperture photometry in practice.

One aperture marks the object and the annulus aperture defines the area for the determination of the background signal around the object, as the Figure 3.5 shows. In that area, the mean value of the brightness of the sky is calculated from the pixel values and then is subtracted from the star's signal. Hence, it is appropriate if there are no other stars in the vicinity of the measured star because the results contain a more significant error. Because of this reason, aperture photometry is not suitable for dense stellar fields, e.g., globular clusters, where many stars are close to each other and measurement of the sky background is very difficult or even impossible.

In the CCD image, we can notice that some of the stars fill a different number of pixels (Figure 3.5), which depends on their brightness and seeing. Therefore, it is also necessary to think about the size of the aperture, which is applied for the star. For photometry, the precision ratio of signal/noise (S/N), which depends on the size of the aperture (Figure 3.6 (a)), is important. As it is shown in the Figure 3.6 (b), a higher ratio of S/N means lower relative uncertainty, thus, higher measurement accuracy. In other words, if we have a dilemma which aperture size is the right-one, we choose that-one which has the lower relative uncertainty as is shown in the Figure 3.6 (b).

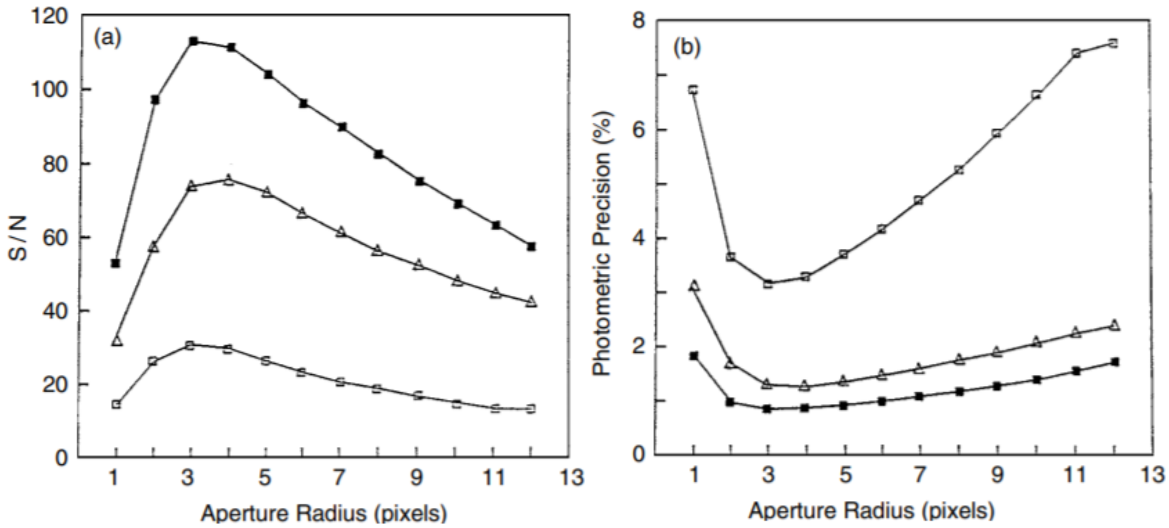


Figure 3.6: Dependence of S/N ratio (a) and relative measurement uncertainty (b) as a function of aperture radius for three stars – ■:V = 14.2 mag, △:V = 14.5 mag, □:V = 16.1 mag. The image scale is 0.4 arc sec per pixel (edited, credit: Howell, 1989).

An atmospheric extinction complicates photometry because it causes changing apparent magnitude during the night without the actual variability of the star (for more information, see sub subsection 3.4.2). That problem can be solved by using *differential photometry.* This method uses a constant apparent magnitude of the so-called comparison star to set up the relative apparent magnitude of the star of our interest with the brightness of this comparison star. Because the differential photometry is usually used in variable stars research, the object of interest is usually denoted as *V – variable star* and as *C – comparison star*. A star close to the V-star with similar colour index and brightness should be chosen as a comparison star. In such case, the atmospheric extinction is strongly reduced and can be neglected.

## 3.4 Sources of errors

### 3.4.1 Photon noise

The amount of fallen photons on the chip's area follow the Poisson distribution, and the $\sigma_\mathrm{p}$ – *photometric error* of one measurement – is inversely proportional to the square root of the number of photons $N$ fallen on the chip, as it is expressed by

$$\sigma_\mathrm{p} \approx \frac{1}{\sqrt{N}}. \tag{3.3}$$

In assumption that differential photometry was used, it is rational to select a brighter stars than a faint stars because a less photometric error occurs.

### 3.4.2 Observing conditions

**Atmospheric extinction**

An atmospheric extinction causes the light scattering and light absorption of the object on the atmosphere particles. It consists of a scattering on molecules and clusters of molecules – the Rayleigh scattering, and a scattering on atoms and particles comparable to the wavelength of radiation – the Mie scattering. The atmospheric extinction is adversely affected by the fact that it is a function of wavelength. Thus, blue light is scattered more than red light. It shows up that the highest extinction is on the horizon, where light must pass longer distance over thicker parts of the atmosphere to the ground. On the other hand, the lowest extinction is in the zenith, because light passes shorter distance to reach a detector. The extinction problem can be reduced by using differential photometry (see subsection 3.3).

**Weather**

Increased humidity in the air causes greater dispersion of light on tiny water particles. Because of the increased dispersion due to the increased humidity causes less photons fall on the area of a chip. Cloudiness makes observation impossible because no light passes through the clouds. The exception is one type of thin, high clouds called cirrus. The light still passes through the cirrus, but it is partially blocked increasing the resulting scatter of the light curve. Temperature changes during observation cause blurring due to the thermal expansion of the material. At night, the temperature is usually lower than during the day, and so the warm rising airflow from the heated ground causes flicker in the air. Even if the telescopes are firmly anchored to their mounting in the ground, a strong wind can move the device slightly, and during long exposure the image may be blurred.

**The Moon**

Moon's diameter is 3,476 km and in the sky occupies approximately 0.5°, which is about the same as the Sun. Presence of the Moon in the night sky during photometry measurements causes increased background and light gradients on the chip, when the Moon is close to the selected object. It is even worse during the full moon phase because its apparent magnitude can reach up to $-12.6$ mag, and such brightness in combination with the Moon's size cause difficulties during observation.

To avoid contamination by the moonlight, it is profitable to check its position at the time of observation in e.g., Object Visibility (Staralt, 2020) programme. All that is needed to do is to enter the day of the observation, longitude and latitude of the observatory, and coordinates of the observed object. The programme then plots a graph which shows when the sunset, sunrise, moonset, moonrise begin, rise and set of the object, culmination of the Moon and the object, and also their distance from each other on the sky – all these information depending on the altitude and universal time.

# *Observation and data processing*

## 4.1 Methodology

As it is known, extra-solar planets orbit various stars with different observable features such as colour index or magnitude. These features affect transit light-curve of the exoplanets, which have their own features e.g., size, orbital period, semi-major axis (for more details see subsection 2.4.4). Thus, the more diverse stars in the image, the better detectability conditions of extra-solar planets can be investigated. Therefore, a relatively dense field of stars for this study is suitable. In assumption that aperture photometry is used, these stars should not be too close to each other (see subsection 3.3).

A light which comes from a source, such as a star, is scattered or absorbed by passing through the Earth's atmosphere (for more details see 3.4.2). The atmospheric extinction is the most pronounced above the horizon, where it causes that from a visible spectrum all wavelengths are scattered, but shorter (blue) wavelengths are scattered more strongly than longer (red) wavelengths. The extinction affects all stars, but each of them differently because of their various *colour index* – it is defined on the basis of star's surface temperature. The colour index can be also determined from the difference between the photometric filters e.g., $B$ and $V$, i.e. $B - V$. Blue hot stars have the highest surface temperatures and low difference between $B - V$, approx. up to the value of 0.3. On the other hand red colder stars have the coolest surface temperatures and the highest difference between $B - V$, approx. from the value of 1 above (Zombeck, 1990). When we know how atmospheric extinction affects the wavelengths of visible spectrum, it is obvious that blue light is scattered the most, thus, objects near the horizon appear reddish than they really are. When stars are at higher altitude, extinction is reduced, and also the colour of the stars is the least affected. Therefore, a *colour test* was needed to be done because I wanted to know, if the depth of transits of the extra-solar planets are detectable in the data, where the trends should be defined by the different colour of the stars and colour extinction.

Each of the stars is specified by its apparent magnitude. A *magnitude test* is associated with it. For this test, stars with different brightness are needed to be selected which have different scattering of the data given by their brightness. The magnitude test is needed to verify in which data (with a given scattering) it is possible to detect the transit of the selected depth. Following the different brightness of these stars, the right exposure time during the observation has to be selected. The reason for this is that saturation can also occur with brighter stars. Because of scattering and absorption, the light does not hit the surface of the chip in such an amount when the object is the lowest above the horizon. On the contrary, most of the light falls on the chip when the object culminates. Therefore, at least one "check" image of the observed object should be taken before the start of the observations, as long as the object is still low above the horizon. The stars which will be selected to photometry measurements should not exceed a certain value given by the dynamic range of the CCD chip (see subsection 3.1) and by this proceeding we can avoid saturation.

Chip of CCD cameras is usually expected to be homogeneous. The different distance of the stars on the chip may affect the photometry, for example due to system defects such as dysfunctional pixels. Homogeneity of the chip can be verified by selecting stars with different distance to the V-star. Another issue may be gradients caused by different illumination of the chip. If the chip is too large, the effects of atmospheric extinction may also occur. A *distance test* is associated with a CCD chip. This test was needed to be done because I wanted to know if the telescope-camera system, brightness gradients and the observation conditions accidentally did not affect the transit detection and did not cause more data scattering and trends.

It is expected that selected stars in the colour, the magnitude and the distance test should have different scattering and also some trends, that definitely affect the detection of extra-solar planets. Moreover, measurements must take place over several nights to ensure different observation conditions (see sub subsection 3.4.2). I selected 3 extra-solar planets with different relative depths of 2%, 1% and 0.57% in order to find out in which types of stars and under what observational conditions we are able to detect an exoplanetary transit. These transits were artificially generated by the software (see subsection 4.4) and then injected to measured data. With the help of another software (see subsection 4.4), I was able to determine in which stars and under what conditions transit could be detected.

One of the categories of objects that meet the conditions of stars diversity and their mutual distance are – *open star clusters*. For photometry measurements, I chose open star cluster in constellation of Perseus – *M34*. The main reasons for the selection of this cluster were the number of the necessary stars with different brightness and colour, and also their relatively sufficient distance from each other. Additional reason for choosing this cluster was its good observability and culmination near the zenith during the months of September and October, when the photometry measurements were done.

## 4.2 Star clusters

A large group of gravitationally bound stars is called *star cluster*. They occur in the galaxies and two types can be distinguish – globular and open star clusters. There are several differences between them.

Globular star clusters have strong gravitational bounding, which give them their well-known spherical shape. They are located in the halo of the galaxy and consist of hundred thousand to million old stars – Population II stars. These clusters have high density of stars – on average about 0.4 stars per cubic parsec, up to 100 or 1000 stars per cubic parsec in the core of the cluster (Elson et al., 1987). Typical distance between the stars is about 1 light year, but in the core, it is up to a few light weeks (ESO.org, 2020). More than 150 globular clusters are already known in the Milky Way Galaxy. A few of the star clusters are observable with naked eye like Omega Centauri or Messier 13 in constellation of Hercules.

Open star clusters have a few hundreds members, much less tightly gravitationally bound and over time, are disrupted by the gravity of giant molecular clouds, other clusters or even by surrounding stars. Open clusters are located in the plane of our galaxy, along the spiral arms and consist of young stars – Population I stars. These stars have a common origin, all are formed from the same giant molecular cloud. Typical density of stars in the centre of open clusters is about 1.5 stars per cubic light year (Nilakshi et al., 2002). There are more than 1000 already known clusters in our galaxy, but the real number can be ten times higher (Dias et al., 2002). The most famous are e.g., Pleiades and Hyades in Taurus constellation, which are also visible with naked eye.

### 4.2.1 Open star cluster M34

Messier 34, also known as M34 or NGC 1039 (Figure 4.1), is located in the constellation of Perseus which is a typical winter constellation for north latitude of 50°. The best observability of M34, which has the right ascension of $02^h42^m05^s$ and declination of $+42°45'43.2''$, is in the months of October, November and December. The cluster can be easily found, because it lies 5° north-west of Algol (Beta Persei). Messier 34 is located at distance 470 parsecs from the Earth, which is 1500 light years (Jones & Prosser, 1996). That distance from M34 makes the $7^{th}$ closest deep sky object to the Earth. A real diameter of M34 is 15 light years, whereas on the night sky spans about $1°10'$. The age of Messier 34 is between 200 – 250 million years (Jones & Prosser, 1996) with 400 members of stars in the range from 0.12 to 1.0 solar masses (Irwin et al., 2006).

Figure 4.1: Image of M34. In the image, hotter stars are blue and colder stars are yellow-red colour (edited, credit: Wikisky, 2020).

## 4.3 Observation

In the beginning, I selected two stars – variable and comparison (this notation comes from the variable stars research). The first criterion for selection of variable and comparison star was that both stars had to be close to each other, because I was not sure if a distance between the stars has an impact on the results. The second criterion was that apparent magnitude of these stars had to be similar, because of scattering in the data. The third criterion was that their difference of colour index had to be as small as possible because I want to minimize the atmospheric extinction. Then I chose 12 stars of which 4 have different magnitude, but similar colour index – the *magnitude test*, (Table 4.1), 4 with similar magnitude, but different colour index – the *colour test*, (Table 4.2) and last 4 with similar magnitude and colour index but different distance to the star marked as variable – the *distance test*, (Table 4.3, Figure 4.2).

The measurements took place at the Observatory of Masaryk University (MUO), which is located on Kraví hora in Brno. The main device of the MUO is a telescope with a diameter of 0.6 m and focal length of 2.78 m, which has a CCD camera G4-16000. Images of Messier 34 were taken in $R$ filter during a 20 seconds exposure time. The object was observed during 3 different nights, because I wanted different observing conditions during each observation (Table 4.4). Observation of M34 during the night 1 (Figure 4.3) started at 17:30 UTC and ended at 1:40 UTC. Observing conditions were poor, e.g., because of increased wind speed (yellow bottom part of the Figure 4.3) and increased cloudiness (red-line dips in the Figure 4.3). Night 2 (Figure 4.4) had better observing conditions than night 1 and observation started at 16:30 UTC, and ended at 2:15 UTC. In the beginning of the night 2 were increased cloudiness (red-line dips in the Figure 4.4). Increased wind speed during the night 2 was almost whole observation (yellow bottom part of the Figure 4.4). Observation of M34 during night 3 (Figure 4.5) started at 16:30 UTC and ended at 23:45 UTC. Clouds did not interfere with the observation, the wind speed was low and stable during the observation.

Table 4.1: The stars selected for the magnitude test. The identification of the stars is according to the catalogue UCAC4 (Zacharias et al., 2012).

| Stars | UCAC4 | $R$ [mag] | $B-V$ [mag] | Right Ascension [$^{\mathrm{h}}$:$^{\mathrm{m}}$:$^{\mathrm{s}}$] | Declination [$^{\circ}$:$'$:$''$] |
|---|---|---|---|---|---|
| Var | 664-012137 | 9.306 | −0.002 | 02:42:13.46 | +42:46:40.6 |
| Comp | 664-012150 | 9.336 | −0.031 | 02:42:22.14 | +42:45:36.6 |
| Check 3 | 665-012220 | 10.544 | 0.137 | 02:41:39.70 | +42:52:45.2 |
| Check 4 | 665-012345 | 11.384 | 0.413 | 02:42:39.06 | +42:49:47.0 |
| Check 12 | 664-012016 | 13.049 | 0.443 | 02:41:29.33 | +42:45:11.6 |
| Check 5 | 664-012261 | 13.604 | 0.560 | 02:43:14.92 | +42:46:05.3 |

Table 4.2: The stars selected for the colour test. The identification of the stars is according to the catalogue UCAC4 (Zacharias et al., 2012).

| Stars | UCAC4 | $R$ [mag] | $B-V$ [mag] | Right Ascension [$^{\mathrm{h}}$:$^{\mathrm{m}}$:$^{\mathrm{s}}$] | Declination [$^{\circ}$:$'$:$''$] |
|---|---|---|---|---|---|
| Var | 664-012137 | 9.306 | −0.002 | 02:42:13.46 | +42:46:40.6 |
| Comp | 664-012150 | 9.336 | −0.031 | 02:42:22.14 | +42:45:36.6 |
| Check 9 | 665-012119 | 9.539 | 0.443 | 02:41:02.65 | +42:54:18.4 |
| Check 2 | 665-012186 | 9.842 | 0.965 | 02:41:25.66 | +42:50:33.3 |
| Check 1 | 665-012279 | 9.536 | 1.184 | 02:42:10.60 | +42:49:56.4 |
| Check 11 | 663-012487 | 9.959 | 1.537 | 02:43:49.98 | +42:33:37.8 |

Table 4.3: The stars selected for the distance test. The identification of the stars is according to the catalogue UCAC4 (Zacharias et al., 2012).

| Stars | UCAC4 | $R$ [mag] | $B-V$ [mag] | Right Ascension [h:m:s] | Declination [°:′:″] | Distance [′] |
|---|---|---|---|---|---|---|
| Var | 664-012137 | 9.306 | −0.002 | 02:42:13.46 | +42:46:40.6 | – |
| Comp | 664-012150 | 9.336 | −0.031 | 02:42:22.14 | +42:45:36.6 | 1.9 |
| Check 7 | 664-012134 | 8.916 | −0.019 | 02:42:13.13 | +42:41:57.1 | 4.7 |
| Check 6 | 663-012214 | 9.116 | 0.042 | 02:41:31.92 | +42:35:39.1 | 13.5 |
| Check 10 | 665-012112 | 9.797 | 0.009 | 02:40:58.94 | +42:52:16.6 | 14.7 |
| Check 8 | 664-012287 | 9.392 | −0.060 | 02:43:32.41 | +42:37:17.5 | 17.3 |

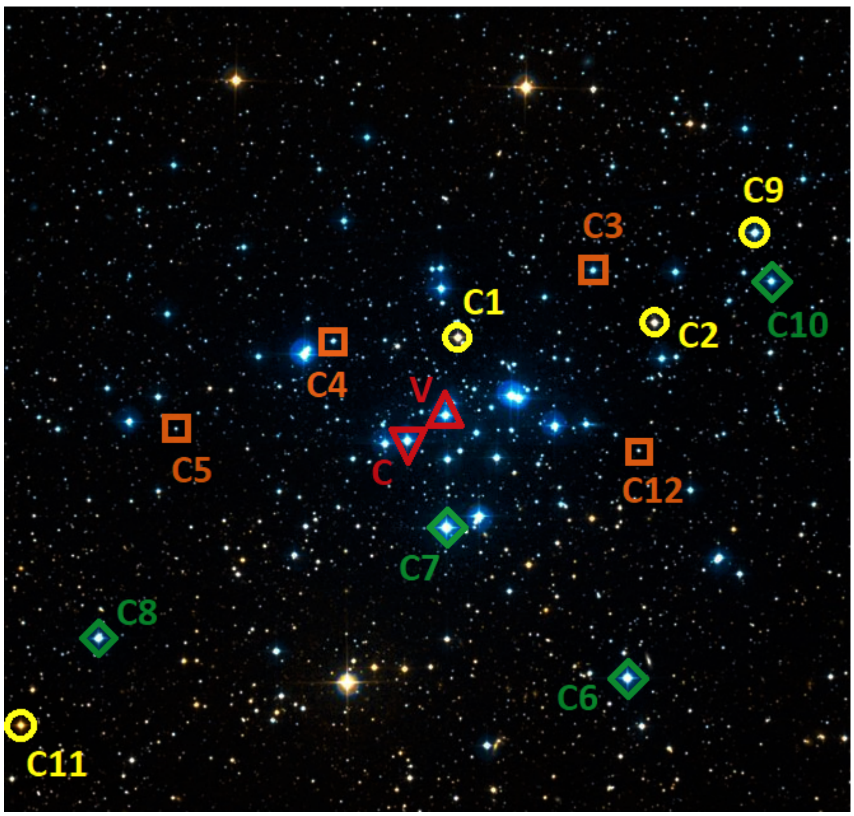


Figure 4.2: Image of M34. Labels are as follows: V – Var, C – Comp, C1 to C13 – Check 1 to Check 13. Stars that belong to the colour test are marked by yellow circles, stars that belong to the magnitude test are marked by orange squares and stars that belong to the distance test are marked by green diamonds (edited, credit: cseligman, 2020).

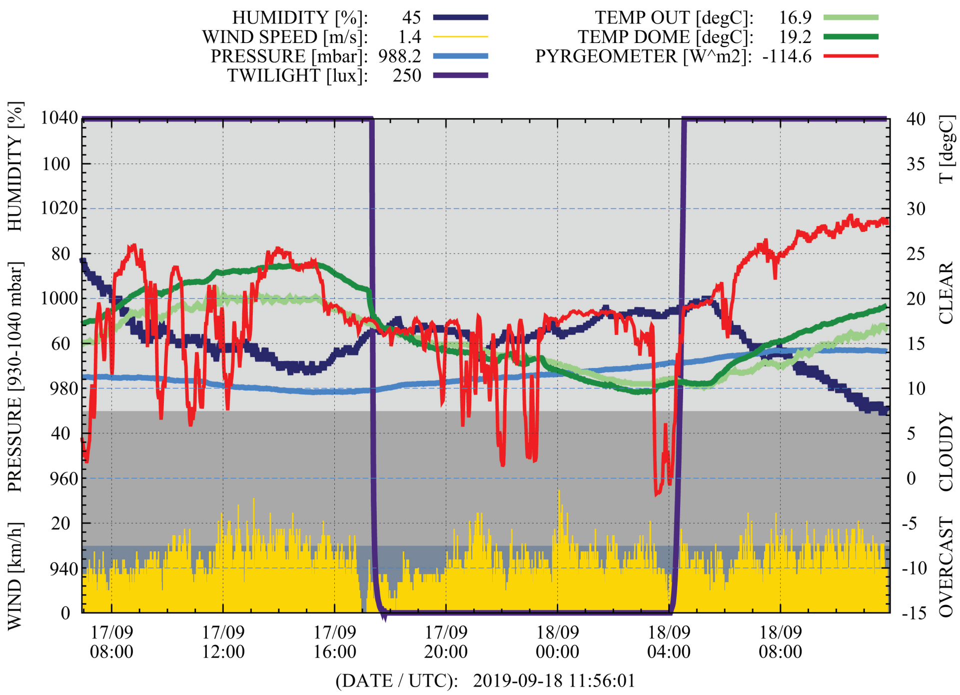


Figure 4.3: Observing conditions during night 1 (credit: astro.physics.muni.cz, 2020).

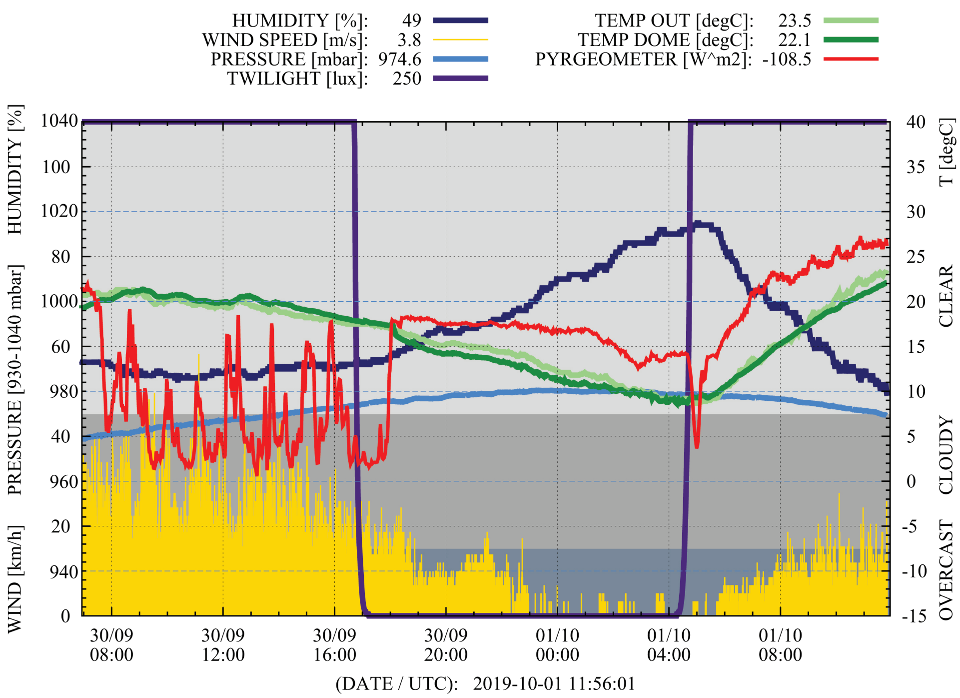


Figure 4.4: Observing conditions during night 2 (credit: astro.physics.muni.cz, 2020).

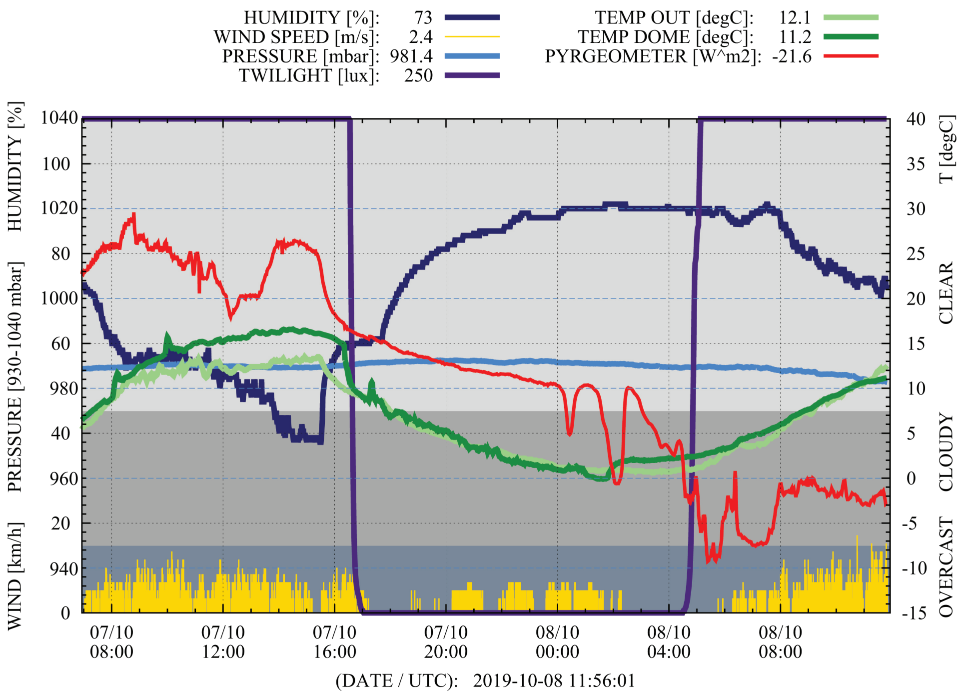


Figure 4.5: Observing conditions during night 3 (credit: astro.physics.muni.cz, 2020).

Table 4.4: Observing conditions, during individual observation nights.

| Observation night | Night 1 17./18.9.2019 | Night 2 30.9./1.10.2019 | Night 3 7./8.10.2019 |
|---|---|---|---|
| Phase of the Moon | 3 days after full moon | new moon | 2 days after first quarter |
| Illuminated part of the Moon | 87% | 0% | 72% |
| Distance of the Moon from M34 | 32° – 34° | – | 100° – 103° |
| Outer temperature | 11°C – 15°C | 15°C – 18°C | 2°C – 8°C |
| Cloudiness | cirrus, cumulus | cloudless night | cumulus |
| Humidity | 60% – 70% | 65% – 90% | 60% – 90% |
| Altitude of M34 at the beginning of observation | 23° | 27° | 30° |
| Maximum elevation of M34 | 84° | 84° | 84° |
| Altitude of M34 at the end of observation | 70° | 57° | 75° |
| Number of frames | 853 | 1133 | 841 |

## 4.4 The used software

**Muniwin**

Aperture differential photometry was done in the Muniwin software, where the raw images were also corrected of the master dark and master flat frames.

**Batman**

Batman is a package in Python and it uses for calculations of exoplanet transit light-curves. Only a few parameters are needed to get a light curve of a transit: orbital period – $P$, planet radius – $R_{\mathrm{p}}$, star radius – $R_{\mathrm{s}}$, semi-major axis – $a$, orbital inclination – $i$, eccentricity – $e$, and easily you get curve of transit.

The main goal of the obtained data from photometry was to find out at which stars it is possible to detect a transit. Therefore, different transits with various depths of 3 exoplanets were injected into measured data sets (Table 4.5), so that we can find out during what observation conditions we are able to detect an extra-solar planet with various depths of transit.

Table 4.5: Parameters of selected extra-solar planets and their parent stars. Transit depth is expressed as $\Delta F$, au is the astronomical unit, $[R_{\mathrm{J}}]$ is the Jupiter radius, $[R_{\mathrm{s}}]$ is stellar radius, $[R_{\mathrm{S}}]$ is the Sun radius and $[^\circ]$ is a degree (exoplanets.org, 2020).

| Exoplanet | GJ 3470 b | XO-2 b | Qatar-1 b |
|---|---|---|---|
| $P$ [days] | $3.336649 \pm 2 \cdot 10^{-6}$ | $2.615857 \pm 5 \cdot 10^{-6}$ | $1.420033 \pm 16 \cdot 10^{-6}$ |
| $a$ [au] | $0.03560 \pm 0.00147$ | $0.03684 \pm 0.00061$ | $0.02343 \pm 0.00039$ |
| $R_{\mathrm{p}}$ $[R_{\mathrm{J}}]$ | $0.374 \pm 0.053$ | $0.983^{+0.029}_{-0.028}$ | $1.164 \pm 0.045$ |
| $R_{\mathrm{s}}$ $[R_{\mathrm{S}}]$ | $0.503 \pm 0.063$ | $0.971^{+0.027}_{-0.026}$ | $0.823 \pm 0.025$ |
| $R_{\mathrm{p}}$ $[R_{\mathrm{s}}]$ | 0.075 | 0.102 | 0.142 |
| $a$ $[R_{\mathrm{s}}]$ | $15.3 \pm 2$ | $8.18 \pm 0.26$ | $6.14 \pm 0.21$ |
| $i$ $[^\circ]$ | $88.12^{+0.34}_{-0.30}$ | $88.90^{+0.60}_{-0.75}$ | $83.47^{+0.40}_{-0.36}$ |
| $e$ | 0 | 0 | 0 |
| $\Delta F$ | $0.00570 \pm 0.00047$ | $0.010800^{+0.000187}_{-0.000177}$ | $0.02120 \pm 0.00045$ |

**PyLightcurve**

PyLightcurve (Tsiaras et al., 2016) is a package in Python used for modeling and analysing transit light-curves. In the data obtained from photometry measurements which already contain artificially injected transit light-curve from Batman, we used Pylightcurve to try to find and fit that transit. PyLightcurve needs the same parameters as Batman for proper transit fit – orbital period, planet radius, star radius, semi-major axis, orbital inclination and eccentricity. Besides that, one extra parameter is needed – mid_time – which is used for estimation an approximate centre of the transit.

## 4.5 Processing methods

Photometric values of the measured stars that were more than $3\sigma$ from the mean value were iteratively removed. Greek letter $\sigma$ is a standard deviation and can be expressed as

$$\sigma = \sqrt{\frac{1}{N} \cdot \sum_{i=1}^{N} (x_\mathrm{i} - \overline{x})^2}, \tag{4.1}$$

where $N$ represents number of measurements in the data set, $x_\mathrm{i}$ represents each value in the data set and $\overline{x}$ is mean of all values in the data set.

The data that were processed by using Batman or PyLightcurve software, required to be transformed by using Pogson's equation

$$\Delta m \equiv m_1 - m_2 = -2.5 \cdot \log \frac{F_1}{F_2}, \tag{4.2}$$

where $m_1$ and $m_2$ are apparent magnitudes of two stars, and $F_1$, and $F_2$ are flux densities of two stars.

Batman software creates theoretical transit in relative fluxes. After generated values of this transit, values are transformed to magnitudes using a formula

$$\Delta m = -2.5 \cdot \log \frac{1}{F_2}, \tag{4.3}$$

and then are inserted into the original photometric data of the measured stars. For the value of $F_1$ the value of 1 is substituted – in Batman software, this value represents areas in the data, where there was no transit. Photometric data set with an artificially created transit are converted to relative fluxes using an equation

$$\frac{F_2}{F_1} = 10^{0.4 \cdot \Delta m}. \tag{4.4}$$

Then these data were inserted into PyLightcurve software which analyses whether the transit is detectable or not. In PyLightcurve software, transit curves are fitted by using Mark Chain Monte Carlo (MCMC) routine.

The examples of the transits that were generated by Batman software and then artificially inserted into the measured data are shown in the Figures 5.1 and 5.2. At the beginning of measured data in the Figure 5.1, an increased scatter of the data is evident due to setting the Moon, which was 2 days after the first quarter phase. Exoplanet with relative transit depth of 0.57% has the smallest depth (Figure 5.1 A), relative transit depth of 1% is the widest (Figure 5.1 B) and relative transit depth of 2% has the highest depth from selected exoplanets (Figure 5.1 C). In the Figure 5.2 A, which represents the magnitude test, is seen that the lower the brightness of the star, the higher scatter is in the data. The Figure 5.2 B shows transits in the colour test, where there can be seen trends caused by colour of the star depending on changing altitude during the night. In the Figure 5.2 C, which represents the results of distance test, can be seen that star a V-K7 saturated during night and some unexpected peaks at stars V-K6, and V-K10 are shown too. At the beginning of Figure 5.2 there is an increased scatter which is caused by the passage of clouds (cirrus clouds) in front of the star cluster and also by increased wind speed. Other graphs can be found in the online material attached to this work.

Transits that were fitted by PyLightcurve software are shown in the Figure 5.3, where V-C is a star with the lowest signal-to-noise ratio and V-K4, V-K12, V-K5 are the stars with the highest signal-to-noise ratio. The Figure 5.3 represents examples of how the correct fit by software PyLightcurve looks like. Other graphs can be found in the online material attached to this work.

The results of magnitude, colour and distance test are shown in the Tables 5.1, 5.2 and 5.3. As a detectable transit was considered that-one, whose fit by PyLightcurve software meet the conditions: the mid_time of the transit should differ from the original value by $+0.02/-0.02$ days and semi-major axis – $a$ – of the exoplanet should not be larger than half of the original value.

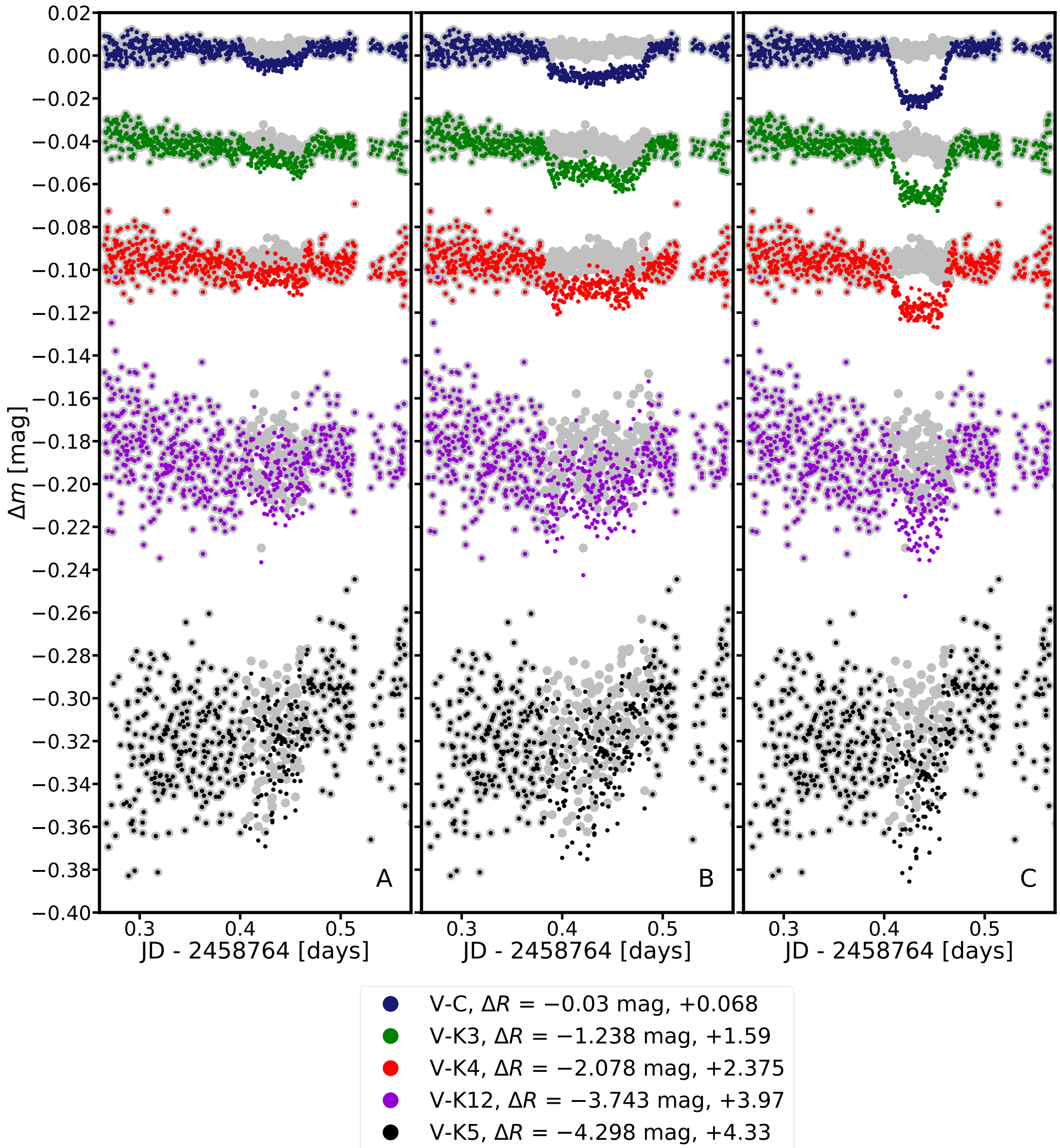


Figure 5.1: Light curves of the stars with artificially injected transit of three exoplanets with different relative depths used for the magnitude test at night 3, A – GJ 3470 b ($\Delta F = 0.0057$), B – XO-2 b ($\Delta F = 0.0108$), C – Qatar-1 b ($\Delta F = 0.0212$).

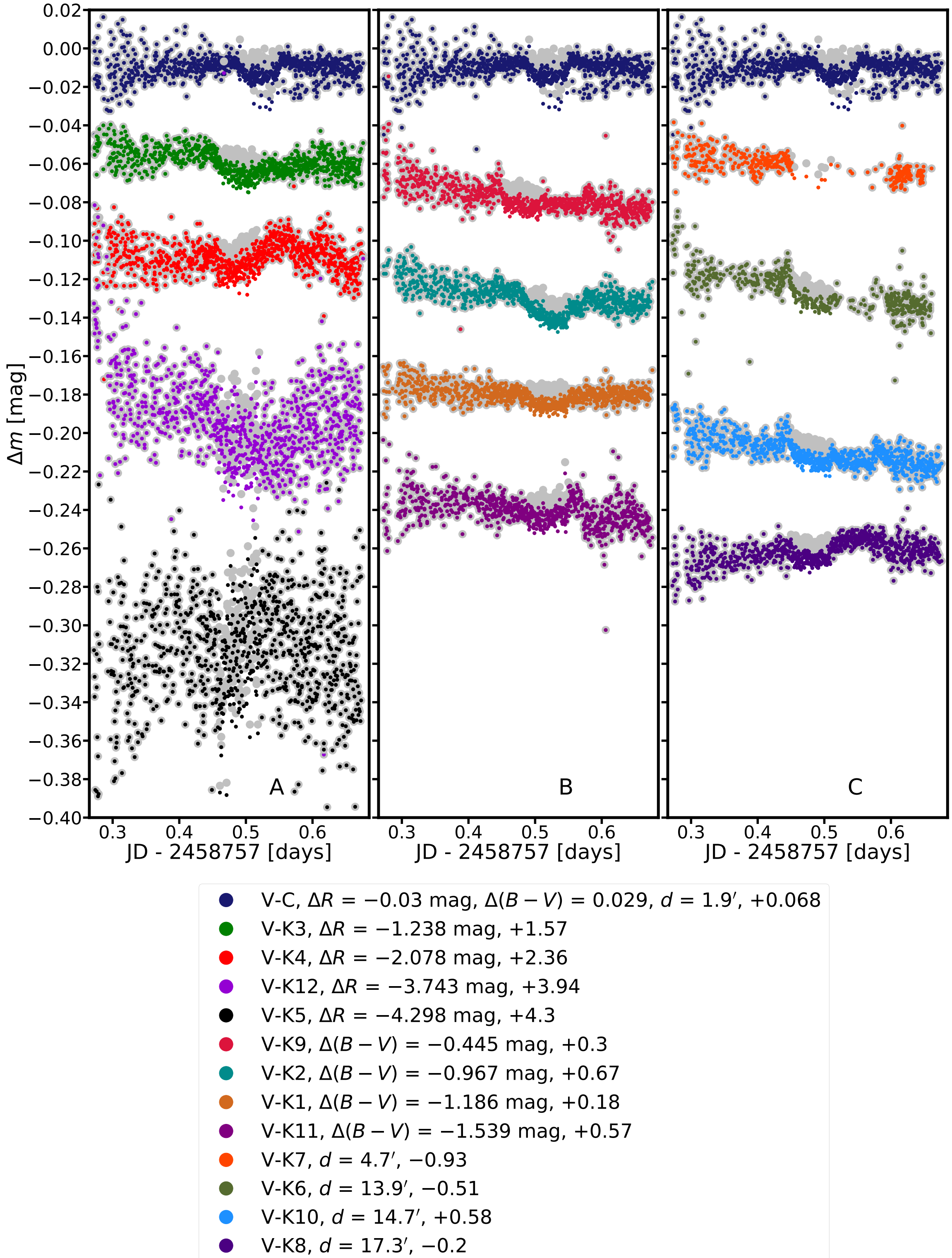


Figure 5.2: Transits of exoplanet GJ 3470 b ($\Delta F = 0.0057$) at the night 2, A – magnitude test, B – colour test, C – distance test.

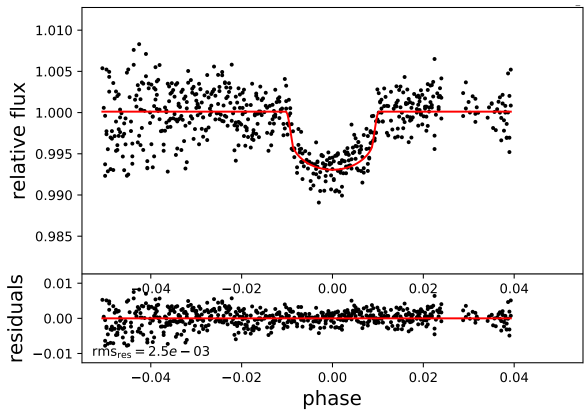


(a) V-C, GJ 3470 b: $R_\mathrm{p}/R_\mathrm{s} = 0.075 \; ^{+0.0080}_{-0.0030}$

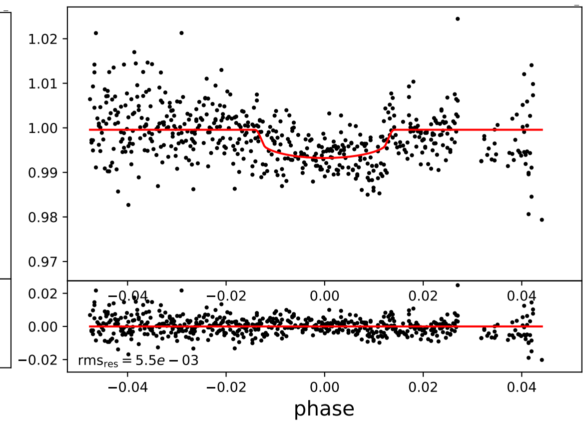


(b) V-K4, GJ 3470 b: $R_\mathrm{p}/R_\mathrm{s} = 0.0711 \; ^{+0.0062}_{-0.0003}$

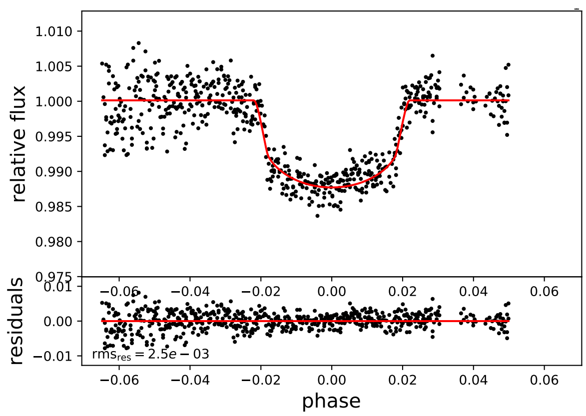


(c) V-C, XO-2 b: $R_\mathrm{p}/R_\mathrm{s} = 0.0996 \; ^{+0.0021}_{-0.0017}$

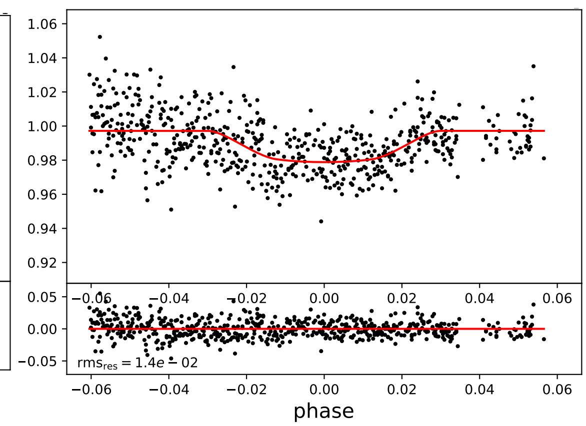


(d) V-K12, XO-2 b: $R_\mathrm{p}/R_\mathrm{s} = 0.13891 \; ^{+0.0001}_{-0.0001}$

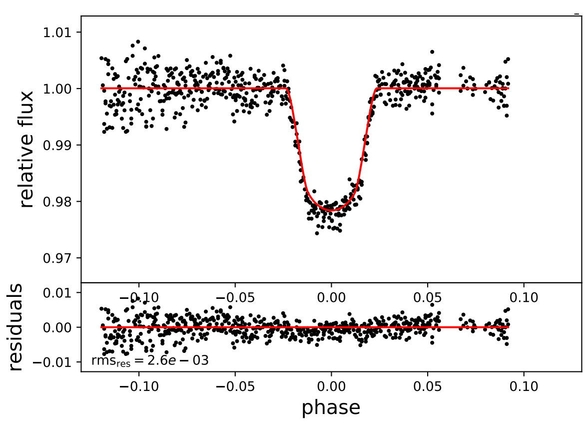


(e) V-C, Qatar-1 b: $R_\mathrm{p}/R_\mathrm{s} = 0.1460 \; ^{+0.0050}_{-0.0040}$

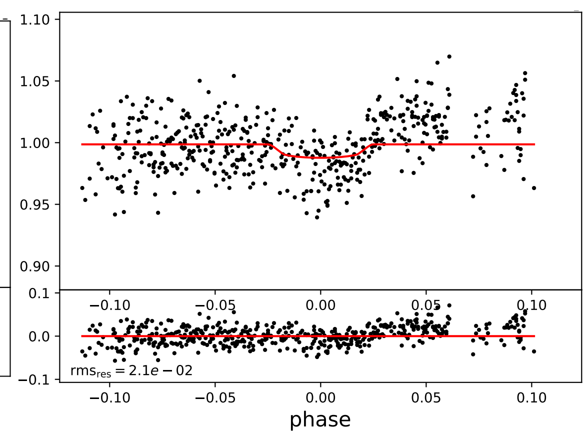


(f) V-K5, Qatar-1 b: $R_\mathrm{p}/R_\mathrm{s} = 0.1276 \; ^{+0.0055}_{-0.0040}$

Figure 5.3: Transits of exoplanets for magnitude test at the night 3.

Table 5.1: The results of the magnitude test. Standard deviation is expressed as $\sigma$. The values in the rows 4, 5, 6 were computed by PyLightcurve, (exoplanets.org, 2020).

| Nights | $\Delta R$ [mag] | $\sigma$ [mag] | GJ 3470 b $R_{\mathrm{p}}/R_{\mathrm{s}} = 0.075$ | XO-2 b $R_{\mathrm{p}}/R_{\mathrm{s}} = 0.102$ | Qatar-1 b $R_{\mathrm{p}}/R_{\mathrm{s}} = 0.142$ |
|---|---|---|---|---|---|
| Night 1 | $-0.03$ V-C | 0.0074 | $0.0653^{+0.0018}_{-0.0008}$ | $0.1019^{+0.0010}_{-0.0013}$ | $0.1400^{+0.0120}_{-0.0070}$ |
| | $-1.238$ V-K3 | 0.0082 | $0.1027^{+0.0006}_{-0.0007}$ | – | $0.1644^{+0.0008}_{-0.0007}$ |
| | $-2.078$ V-K4 | 0.0105 | – | – | $0.1447^{+0.0005}_{-0.0694}$ |
| | $-3.743$ V-K12 | 0.0272 | – | – | $0.1036^{+0.0002}_{-0.0001}$ |
| | $-4.298$ V-K5 | 0.0428 | – | – | $0.1663^{+0.0510}_{-0.0017}$ |
| Night 2 | $-0.03$ V-C | 0.0032 | $0.0600^{+0.0630}_{-0.0020}$ | $0.0907^{+0.0012}_{-0.0007}$ | $0.1330^{+0.0014}_{-0.0018}$ |
| | $-1.238$ V-K3 | 0.0059 | $0.0830^{+0.0150}_{-0.0020}$ | $0.1261^{+0.0002}_{-0.0005}$ | $0.1613^{+0.0004}_{-0.0005}$ |
| | $-2.078$ V-K4 | 0.0076 | $0.0840^{+0.0680}_{-0.0030}$ | $0.1035^{+0.0077}_{-0.0012}$ | $0.1490^{+0.0141}_{-0.0000}$ |
| | $-3.743$ V-K12 | 0.0214 | – | – | $0.1627^{+0.0001}_{-0.0092}$ |
| | $-4.298$ V-K5 | 0.0282 | – | – | $0.1230^{+0.0070}_{-0.0060}$ |
| Night 3 | $-0.03$ V-C | 0.0022 | $0.0750^{+0.0080}_{-0.0030}$ | $0.0996^{+0.0021}_{-0.0017}$ | $0.1460^{+0.0050}_{-0.0040}$ |
| | $-1.238$ V-K3 | 0.0047 | $0.0881^{+0.0012}_{-0.0007}$ | $0.1120^{+0.0007}_{-0.0014}$ | $0.1472^{+0.0005}_{-0.0005}$ |
| | $-2.078$ V-K4 | 0.0060 | $0.0711^{+0.0062}_{-0.0003}$ | $0.1145^{+0.0003}_{-0.0004}$ | $0.1410^{+0.0005}_{-0.0003}$ |
| | $-3.743$ V-K12 | 0.0160 | – | $0.1390^{+0.0001}_{-0.0001}$ | $0.1447^{+0.0002}_{-0.0002}$ |
| | $-4.298$ V-K5 | 0.0244 | – | – | $0.1276^{+0.0055}_{-0.0040}$ |

Table 5.2: The results of the colour test. Standard deviation is expressed as $\sigma$. The values in the rows 4, 5, 6 were computed by PyLightcurve, (exoplanets.org, 2020).

| Nights | $B-V$ [mag] | $\sigma$ [mag] | GJ 3470 b $R_p/R_s = 0.075$ | XO-2 b $R_p/R_s = 0.102$ | Qatar-1 b $R_p/R_s = 0.142$ |
|---|---|---|---|---|---|
| Night 1 | 0.029 V-C | 0.0074 | $0.0653^{+0.0018}_{-0.0008}$ | $0.1019^{+0.0010}_{-0.0013}$ | $0.1400^{+0.0120}_{-0.0070}$ |
| | $-0.445$ V-K9 | 0.0100 | – | – | $0.1768^{+0.0005}_{-0.0007}$ |
| | $-0.967$ V-K2 | 0.0092 | – | – | $0.1714^{+0.0007}_{-0.0028}$ |
| | $-1.186$ V-K1 | 0.0088 | $0.1180^{+0.0020}_{-0.0560}$ | $0.1188^{+0.0005}_{-0.0005}$ | $0.1606^{+0.0009}_{-0.0161}$ |
| | $-1.539$ V-K11 | 0.0130 | $0.0917^{+0.0013}_{-0.0009}$ | $0.1109^{+0.0005}_{-0.0004}$ | $0.1431^{+0.0018}_{-0.0005}$ |
| Night 2 | 0.029 V-C | 0.0032 | $0.0600^{+0.0630}_{-0.0020}$ | $0.0907^{+0.0012}_{-0.0007}$ | $0.1330^{+0.0014}_{-0.0018}$ |
| | $-0.445$ V-K9 | 0.0073 | – | $0.1085^{+0.0014}_{-0.0012}$ | $0.1350^{+0.0030}_{-0.0020}$ |
| | $-0.967$ V-K2 | 0.0067 | – | $0.1240^{+0.0030}_{-0.0060}$ | $0.1719^{+0.0015}_{-0.0026}$ |
| | $-1.186$ V-K1 | 0.0041 | $0.0867^{+0.0015}_{-0.0017}$ | $0.1060^{+0.0019}_{-0.0024}$ | $0.1469^{+0.0020}_{-0.0128}$ |
| | $-1.539$ V-K11 | 0.0075 | – | $0.0980^{+0.0020}_{-0.0050}$ | $0.1320^{+0.0070}_{-0.0060}$ |
| Night 3 | 0.029 V-C | 0.0022 | $0.0750^{+0.0080}_{-0.0030}$ | $0.0996^{+0.0021}_{-0.0017}$ | $0.1460^{+0.0050}_{-0.0040}$ |
| | $-0.445$ V-K9 | 0.0048 | – | $0.1150^{+0.0015}_{-0.0020}$ | $0.1495^{+0.0014}_{-0.0021}$ |
| | $-0.967$ V-K2 | 0.0055 | – | $0.1165^{+0.0007}_{-0.0012}$ | $0.1557^{+0.0009}_{-0.0019}$ |
| | $-1.186$ V-K1 | 0.0040 | $0.1046^{+0.0017}_{-0.0042}$ | $0.1300^{+0.0019}_{-0.0028}$ | $0.1590^{+0.0030}_{-0.0020}$ |
| | $-1.539$ V-K11 | 0.0066 | – | $0.1400^{+0.0400}_{-0.0200}$ | $0.1750^{+0.0017}_{-0.0051}$ |

Table 5.3: The results of the distance test. Standard deviation is expressed as $\sigma$. The values in the rows 4, 5, 6 were computed by PyLightcurve. Distance from the V-star is marked as $d$. During night 3, the star K7 saturated and hence is not in the Table, (exoplanets.org, 2020).

| Nights | $d$ [′] | $\sigma$ [mag] | GJ 3470 b $R_\mathrm{p}/R_\mathrm{s} = 0.075$ | XO-2 b $R_\mathrm{p}/R_\mathrm{s} = 0.102$ | Qatar-1 b $R_\mathrm{p}/R_\mathrm{s} = 0.142$ |
|---|---|---|---|---|---|
| Night 1 | 1.9 V-C | 0.0074 | $0.0653^{+0.0018}_{-0.0008}$ | $0.1019^{+0.0010}_{-0.0013}$ | $0.1400^{+0.0120}_{-0.0070}$ |
| | 4.7 V-K7 | 0.0094 | $0.0919^{+0.0025}_{-0.0012}$ | – | $0.1638^{+0.0013}_{-0.0036}$ |
| | 13.9 V-K6 | 0.0081 | – | – | $0.1744^{+0.0008}_{-0.0011}$ |
| | 14.7 V-K10 | 0.0086 | – | – | $0.1703^{+0.0007}_{-0.0493}$ |
| | 17.3 V-K8 | 0.0095 | $0.0870^{+0.0050}_{-0.0160}$ | $0.1043^{+0.0222}_{-0.0005}$ | $0.1548^{+0.0008}_{-0.0009}$ |
| Night 2 | 1.9 V-C | 0.0032 | $0.0600^{+0.0630}_{-0.0020}$ | $0.0907^{+0.0012}_{-0.0007}$ | $0.1330^{+0.0014}_{-0.0018}$ |
| | 4.7 V-K7 | 0.0076 | – | – | $0.1340^{+0.0120}_{-0.0060}$ |
| | 13.9 V-K6 | 0.0079 | – | – | $0.1330^{+0.0180}_{-0.0140}$ |
| | 14.7 V-K10 | 0.0077 | – | $0.1109^{+0.0014}_{-0.0020}$ | $0.1380^{+0.0520}_{-0.0020}$ |
| | 17.3 V-K8 | 0.0060 | $0.0870^{+0.0120}_{-0.0049}$ | $0.0920^{+0.0240}_{-0.0030}$ | $0.1270^{+0.0030}_{-0.0018}$ |
| Night 3 | 1.9 V-C | 0.0022 | $0.0750^{+0.0080}_{-0.0030}$ | $0.0996^{+0.0021}_{-0.0017}$ | $0.1460^{+0.0050}_{-0.0040}$ |
| | 13.9 V-K6 | 0.0038 | $0.0760^{+0.0080}_{-0.0040}$ | $0.1050^{+0.0040}_{-0.0030}$ | $0.1470^{+0.0180}_{-0.0110}$ |
| | 14.7 V-K10 | 0.0044 | $0.0672^{+0.0108}_{-0.0015}$ | $0.1080^{+0.0160}_{-0.0050}$ | $0.1430^{+0.0030}_{-0.0030}$ |
| | 17.3 V-K8 | 0.0053 | $0.0900^{+0.0080}_{-0.0270}$ | $0.1060^{+0.0030}_{-0.0040}$ | $0.1400^{+0.0600}_{-0.0400}$ |

# *Discussion and Conclusions*

It is not impossible to detect extra-solar planets using ground-based telescopes. However, the Earth's atmosphere can affect transit detection to a large scale compared to space-based telescopes. Observation conditions are, therefore, an inseparable part of successful transit detection. In order to ensure different observation conditions and, thus, find out which of observing conditions most affect the detection of transit, observation took place over three nights (Table 4.4, Figures 4.3, 4.4 and 4.5). The obtained values, at least from the beginning of the night, are also affected by the altitude of the object at the time of the beginning of the observation. The lower altitude of the object above the horizon, the greater signal-to-noise ratio is in the data. The occurrence of the Moon in the sky and light pollution cause an increased gradient of illumination on the chip.

As we know, extra-solar planets orbit stars with different brightness or colour index. Different brightness of stars causes different scattering in the data and the colour of the star depending on the changing altitude causes trends. Moreover, the Moon and light pollution can cause uneven illumination of the chip. Therefore, the magnitude, the colour and the distance test was done, whose results show how the selection of different and differently distant stars on the chip affects the detection of transit. The open star cluster M34 was chosen for CCD photometry due to the diversity of the stars, their sufficient distance from each other and the high culmination at the time of observation. Transits with relative depths of 2%, 1% and 0.57% were generated in Batman software (see subsection 4.4) and then the transits were artificially inserted into the measured data. These data (with inserted transits) were imported to PyLightcurve software (see subsection 4.4), in order to detect and fit these transits.

From the obtained data set the best night for observation was the night 3 (Table 4.4 and Figure 4.5), although the Moon was 2 days after the first quarter. Otherwise the absence of the Moon in the sky during the observation seems to be important (due to increased sky background illumination), but factors such as the signal-to-noise ratio, stability of wind speed and direction, and atmospheric pressure are much more important. The Figures 4.3, 4.4 and 4.5 show that the best signal-to-noise ratio due to seeing, and the most stable pressure values, and the wind speed had the night 3. These conditions have a significant effect on the data results. Thus, the obtained values from the night 3 are much better compared to the night 1 and the night 2. Similarly, the altitude of the star cluster at the beginning of the observation was the highest compared to the night 1 and the night 2, hence, the increased scatter of the data is not evident in the graphs.

The magnitude test should show how the signal-to-noise ratio and, thus, the scatter of the data depending on the different brightness of the stars. Stars with different apparent magnitude (9 mag – 13.6 mag) but similar colour index (Table 4.1) were selected for this test. The results of the magnitude test (Table 5.1) show that increasing star's apparent magnitude causes higher scatter in data and then, the accuracy of the determination of $R_\mathrm{p}/R_\mathrm{s}$ decreases. An interesting result is that an exoplanet with a relative transit depth of 1%, (which is not the smallest compared to 0.57%) was not detected during the night 1 in 4 out of 5 cases. This is due to the fact that cloudiness was increased during the night 1 and also because transit with a relative depth of 1% is the widest of the selected exoplanets (0.11 days), thus, transit was hard to be detected by PyLightcurve software (see subsection 4.4). During the night 2 and the night 3, transits with relative depths of 1% and 0.57%

were not detected at some stars due to increased scatter in data. An exoplanet with a relative transit depth of 2% was detected in the magnitude test at all three nights even at star with brightness of 13.6 mag with scatter in data of value 0.0428 mag.

The colour test should show how the detection of the transit can be affected by the different colour of the stars depending on the changing altitude during the night. Therefore, stars with different colour index (0.4 mag – 1.5 mag) but similar brightness (Table 4.2) were selected for this test. The worst detected exoplanetary transit was the one with a relative transit depth of 0.57% during each night, mainly due to its depth of transit, and also due to bad observing conditions. An exoplanet with a relative transit depth of 1% was not detected only in 2 cases (V-K2, V-K9) during the night 1 (Table 4.2). It was due to the fact that the transit occurred behind the area where the clouds stopped interfering with the observation and PyLightcurve software had a problem to fit that transit, which is also due to the increased scatter in data. An exoplanet with a relative transit depth of 2% was detected at all three nights even at star with colour index of 1.537 mag with scatter in data of value 0.0130 mag.

The distance test should verified how the gradient of the chip's illumination caused by the Moon or light pollution affects detectability of the transit. For this test, stars with different distances on the chip ($4.7' - 17.3'$) but similar brightness and colour index (Table 4.3) were selected. An exoplanet with a relative transit depth of 0.57% could not be detected especially during night 2 (Table 5.3). The night 2 had better observing conditions than the night 1 and also less scatter in the data, but at the night 2 a star V-K7 saturated during the measurement and unexpected peaks occurred at stars V-K6 and V-K10 (Table 4.3 C). The exoplanet with a relative transit depth of 1 % was not detectable during the night 1 and the night 2 mainly due to the width of its transit (0.11 days) in places where it was no longer cloudy, and also because of the greater scatter in data. An exoplanet with a relative transit depth of 2% was detected during all three nights at each star.

The results show that transit detection is not affected by the colour of the star or the distance of the star on the chip. However, the detectable transit is clearly affected by the signal-to-noise ratio caused by seeing and the observing conditions, the stability of the wind speed and the atmospheric pressure in particular.

# *References*

Alibert, Y., & Benz, W. 2017, Astronomy and Astrophysics, 598, L5

Babcock, H. W. 1953, Publications of the Astronomical Society of the Pacific, 65, 229

Bond, I. A., Udalski, A., Jaroszyński, M., et al. 2004, The Astrophysical Journal, 606, L155

Boss, A. P. 2001, Lunar and Planetary Science Conference, 1193

Boyle, W. S., & Smith, G. E. 1970, Charge coupled semiconductor devices, Bell System Technical Journal

Cassan, A., Kubas, D., Beaulieu, J.-P., et al. 2012, Nature, 481, 167

D'Angelo, G., & Bodenheimer, P. 2016, The Astrophysical Journal, 828, 33

Dias, W. S., Alessi, B. S., Moitinho, A., et al. 2002, Astronomy and Astrophysics, 389, 871

Einstein, A. 1936, Science, 84, 506

Elson, R., Hut, P., & Inagaki, S. 1987, Annual Review of Astronomy and Astrophysics, 25, 565

Howell, S. B. 1989, Two-dimensional aperture photometry - Signal-to-noise ratio of pointsource observations and optimal data-extraction techniques, PASP, 101, 616

Howell, S. B. 2006, Handbook of CCD Astronomy, Cambridge University Press `https://epdf.pub/handbook-of-ccd-astronomy-cambridge-observing-handbooks-for-research-astronomers-pdf-5eccd0c015b18.html`

Irwin, J., Aigrain, S., Hodgkin, S., et al. 2006, Monthly Notices of the Royal Astronomical Society, 370, 954

Jones, B. F., & Prosser, C. F. 1996, Astronomical Journal, 111, 1193

Lagrange, A.-M., Gratadour, D., Chauvin, G., et al. 2009, Astronomy and Astrophysics, 493, L21

Léger, A., Rouan, D., Schneider, J., et al. 2009, Astronomy and Astrophysics, 506, 287-302

Lloyd, R. 2001, Free-Floating Planets – British Team Restakes Dubious Claim `http://www.space.com/scienceastronomy/astronomy/free_floaters_010403-1.html`

Marois, C., Macintosh, B., Barman, T., et al. 2008, Science, 322, 1348

Mayor, M., & Queloz, D. 1995, Nature, 378, 355

Mighell, K. J. 1999, Astronomical Data Analysis Software and Systems VIII, 317

Newton, I., & Cotes, R. 1713, Philosophiae Naturalis Principia Mathematica. Auctore Isaaco Newtono

Nilakshi, Sagar, R., Pandey, A. K., et al. 2002, Astronomy and Astrophysics, 383, 153

Rix, H.-W., & Bovy, J. 2013, The Astronomy and Astrophysics Review, 21, 61

Sahlmann, J., Lazorenko, P. F., Ségransan, D., et al. 2013, Astronomy and Astrophysics, 556, A133

Sumi, T., Kamiya, K., Bennett, D. P., et al. 2011, Nature, 473, 349

Thorsett, S. E., Arzoumanian, Z., & Taylor, J. H. 1993, Astrophysical Journal Letters, 412, L33

Tsiaras, A., Waldmann, I. P., Rocchetto, M., et al. 2016, Astrophysics Source Code Library

Woolfson, M. M. 1993, Quarterly Journal of the Royal Astronomical Society, 34, 1

Yin, Q., Jacobsen, S. B., Yamashita, K., et al. 2002, Nature, 418, 949

Zacharias, N., Finch, C. T., Girard, T. M., et al. 2012, VizieR Online Data Catalog, I/322A

Zombeck, M. V. 1990, Cambridge: University Press

## *Electronic sources*

https://www.eso.org/public/news/eso0107/

https://exoplanets.nasa.gov

http://astrin.planetarium.sk/extrasolarne-planety-vii-priame-zobrazenie-c07108

https://www.space.com/31497-exoplanets-direct-imaging-next-big-thing.html

https://www.esa.int/ESA_Multimedia/Images/2019/02/Detecting_exoplanets_with_transits

https://www.esa.int/ESA_Multimedia/Images/2019/02/Detecting_exoplanets_with_radial_velocity

https://www.esa.int/ESA_Multimedia/Images/2019/02/Detecting_exoplanets_with_microlensing

https://hubblesite.org/contents/media/images/1995/45/361-Image.html?news=true https://www.nasa.gov/feature/goddard/2020/goldilocks-stars-are-best-places-to-look-for-life

https://www.gxccd.com/art?id=303&lang=409

http://wikisky.org

http://catserver.ing.iac.es/staralt/

https://cseligman.com/text/atlas/ngc10.htm#1039

http://hvezdy.astro.cz/exoplanety/49-historicke-zastaveni

https://asd.gsfc.nasa.gov/blueshift/index.php/2015/07/22/how-many-stars-in-the-milky-way/

http://exoplanets.org/table

https://astro.physics.muni.cz/meteo